

# Zinc-based metal halide electrolytes for all-solid-state zinc-metal batteries

Received: 9 March 2025

Accepted: 2 January 2026

Published online: 19 January 2026

Check for updates

Sanlue Hu<sup>1,2,5</sup>, Caiyun Chang<sup>1,2,5</sup>, Yang-Peng Lin<sup>3,4,5</sup>, Jie Li<sup>1,2</sup>, Dun Wang<sup>1,2</sup>,  
Xuexia Lu<sup>3</sup>, Ke-Zhao Du<sup>3</sup>✉, Hui-Ming Cheng<sup>1,2</sup>✉ & Cuiping Han<sup>2</sup>✉

The advancement of electrolyte materials is fundamental to the advancement of batteries. While zinc-metal batteries offer compelling advantages in safety, cost, and environmental sustainability, their performance is constrained by conventional aqueous electrolytes. All-solid-state zinc-ion electrolytes, which can inherently address the issues associated with aqueous electrolytes, are promising but yet currently in their nascent stages. Here, we show a composition engineering strategy to design metal halide-based zinc-ion electrolytes, and two types of zinc-based hybrid metal halides,  $C_4N_2H_{12}ZnBr_4$  and  $C_4N_2H_{12}ZnCl_4$ , are obtained. Both solid-state electrolytes exhibit good electronically insulating properties and low zinc-migration energy barriers.  $C_4N_2H_{12}ZnBr_4$  demonstrates a high ionic conductivity of  $2.9 \times 10^{-4} \text{ S cm}^{-1}$  at 25 °C and a wide electrochemical window of  $\sim 3.74 \text{ V}$ , making it suitable for all-solid-state zinc-metal batteries. The  $C_4N_2H_{12}ZnBr_4$  electrolyte also establishes a tight contact with the zinc electrode, thereby minimizing interface resistance for enhanced electrochemical performance. As a result, an all-solid-state Zn ||  $I_2$  cell using  $C_4N_2H_{12}ZnBr_4$  electrolyte achieves a high capacity retention of  $234.5 \text{ mAh g}^{-1}$  after 200 cycles at  $0.2 \text{ mA cm}^{-2}$ , with a low capacity degradation rate of 0.056% per cycle. This work provides a design approach for metal halide-based solid electrolytes in zinc-metal batteries.

In recent years, increasing renewable energy production has highlighted the imperative to advance battery technology, with a particular emphasis on alternatives beyond lithium-ion batteries<sup>1</sup>. Electrolyte materials, which serve as a key medium for ion transport between negative electrode and positive electrode, play a critical role in battery devices, and battery performance is heavily influenced by the properties of electrolytes. Among various new battery systems, aqueous zinc-metal batteries (ZMBs) become a hot topic due to their high volumetric capacity ( $5855 \text{ mAh cm}^{-3}$ ), inherent safety, cost-effectiveness, and environmental sustainability<sup>2,3</sup>. Nevertheless, the wide application of aqueous ZMBs has not been achieved due to the

inherent high activity of aqueous electrolytes<sup>4-6</sup>, the narrow electrochemical stability window, and the dissolution of positive electrode materials<sup>7,8</sup>.

Solid-state electrolytes are promising alternatives to aqueous electrolytes due to their potential advantages of safety, energy density, and mechanical properties<sup>9</sup>. It is very exciting that the introduction of solid-state electrolytes can effectively address the issues of dendrite formation and gas generation associated with zinc negative electrodes in aqueous ZMBs. Inspired by the research of lithium-ion batteries, most studies on solid-state zinc-ion electrolytes are based on polymer electrolyte materials<sup>10,11</sup>. Unfortunately, the ionic conductivity of

<sup>1</sup>Shenzhen Key Laboratory of Energy Materials for Carbon Neutrality, Institute of Technology for Carbon Neutrality, Shenzhen Institute of Advanced Technology, Chinese Academy of Sciences, Shenzhen, China. <sup>2</sup>Faculty of Materials Science and Energy Engineering, Shenzhen University of Advanced Technology, Shenzhen, China. <sup>3</sup>College of Chemistry and Materials Science, Fujian Provincial Key Laboratory of Advanced Materials Oriented Chemical Engineering, Fujian Normal University, Fuzhou, China. <sup>4</sup>Xiamen Institute of Environmental Science, Xiamen, China. <sup>5</sup>These authors contributed equally: Sanlue Hu, Caiyun Chang, Yang-Peng Lin. ✉e-mail: [duke@fjnu.edu.cn](mailto:duke@fjnu.edu.cn); [hm.cheng@siat.ac.cn](mailto:hm.cheng@siat.ac.cn); [cp.han@siat.ac.cn](mailto:cp.han@siat.ac.cn); [hancuiping@suat-sz.edu.cn](mailto:hancuiping@suat-sz.edu.cn)

polymer electrolytes, which relies on the random thermal motion of zinc ions, is relatively low. Zinc ions present significant challenges for solid-state migration due to two key properties: their high charge valence (+2) and relatively low electronegativity (1.65). The high charge density associated with the +2 state induces strong electrostatic interactions with the anion lattice, resulting in high migration barriers. Simultaneously, the low electronegativity promotes stronger bonding with anions (e.g.,  $O^{2-}$ ), which further restricts mobility. This dual impediment makes zinc ion conduction particularly difficult to achieve in solid electrolytes. Recently, inorganic-based solid-state zinc-ion electrolytes have been developed, such as fluorine-doped mesoporous zinc sulfide  $Zn_3S_{1-x}F_x$ <sup>12</sup> and a phosphorus sulfide  $ZnPS_3$ <sup>13</sup>. These inorganic-based solid-state zinc-ion electrolytes possess high ionic conductivity and can effectively conduct zinc ions, endowing their batteries with good cycling performance. However, the research of solid-state zinc-ion electrolytes is still in its early stages, thereby the quest for applicable solid-state electrolytes remains of significant importance.

In this work, we proposed a composition engineering strategy for designing metal halide-based all-solid-state zinc-ion electrolytes. Based on the theoretical analysis between lithium- and zinc-based ternary metal halides, two zinc-based hybrid metal halides,  $C_4N_2H_{12}ZnBr_4$  and  $C_4N_2H_{12}ZnCl_4$  (denoted as PipZnBr<sub>4</sub> and PipZnCl<sub>4</sub>, respectively, where Pip is the divalent ion of piperazine), were theoretically studied. These two materials show good electronically insulating properties and low zinc-migration barriers and may have the potential to be all-solid-state zinc-ion electrolytes. PipZnBr<sub>4</sub>, in particular, was experimentally verified and found to have high ionic conductivity, low activation energy, and a wide electrochemical window. It also forms a close contact with the zinc electrode to reduce interface resistance for promising electrochemical performance.

## Results

### Rational design of hybrid metal halides as all-solid-state zinc-ion electrolytes

Metal halide materials, a large family of materials composed of metal and halide ions (like chloride or bromide), have been widely used in various fields<sup>14–17</sup>. There are successful examples of metal halide materials for lithium solid electrolytes<sup>18,19</sup>. These studies verify that metal halide materials show good structural stability, high ionic conductivity, wide voltage windows, and long cycle stability at high voltages. The attempt to introduce metal halides into ZMBs is of great significance, as it can not only enrich the types of all-solid-state zinc-ion electrolyte materials but also deepen our understanding of their intrinsic mechanisms. However, it was found that metal halide materials for solid-state lithium batteries cannot be directly applicable to ZMBs. Specifically, lithium (Li) is the 3rd element and belongs to alkali metals, while zinc (Zn) is the 30th element and belongs to the transition metals. As shown in Fig. 1a, b and Supplementary Fig. 1, in the arrangement of electrons outside nucleus, Li ions have significantly fewer electrons than Zn ions. When Li or Zn elements are combined with halogen elements, both Li and Zn can usually form tetrahedral structures and octahedral ligand structures (Fig. 1c, d). When the coordination environments of Li and Zn ions with halogens are either 4-coordinated or 6-coordinated (Li/Zn surrounded by 4 or 6 halide atoms), their ionic radii are notably similar. In a four-coordination condition, the radius of  $Li^+$  is 59 pm, and that of  $Zn^{2+}$  is 60 pm; in a six-coordination condition, the radius of  $Li^+$  is 76 pm and that of  $Zn^{2+}$  is 74 pm<sup>20</sup>. This similarity implies that they occupy similar space in the crystal. To understand why these structurally similar materials behave differently as electrolytes, a comparative analysis of the tetrahedral and octahedral structures of Li and Zn at the orbital level was performed to elucidate their similarities and differences. As shown in Supplementary Figs. 2–5 (Supplementary Data 1), when Li and Zn atoms bond with halogen atoms to form tetrahedral or octahedral

structures, the nature of their interaction differs fundamentally. The electron orbitals of Li and halogen atoms exhibit clear separation, with minimal overlap between their electron clouds (Supplementary Figs. 2 and 3). This result means Li and halogen atoms retain a non-bonding state in their elemental orbitals, which suggests that the predominant binding mode between Li ions and halogens is ionic bonds. Conversely, when Zn ions coordinate with halogens to form tetrahedral or octahedral structures, their interaction exhibits stronger orbital overlap (Supplementary Figs. 4 and 5). This overlap electron cloud sharing generates distinct bonding and antibonding states, which means a covalent character in the Zn-halogen bond. To quantify the interaction, an in-depth analysis of the crystal orbital bond index (COBI)<sup>21</sup> was conducted for Li–Cl and Zn–Cl as representative cases (Supplementary Data 2). As illustrated in Supplementary Fig. 6, the COBI values for 4-coordinated and 6-coordinated LiCl are 0.15 and 0.09, respectively, suggesting a strong ionic character. In contrast, the COBI values for 4-coordinated and 6-coordinated  $ZnCl_2$  are 0.22 and 0.18 (Supplementary Fig. 7), indicating a stronger covalent interaction between Zn and the halogens. These results suggest that the Li-based halides characterized by localized ionic bonding, which could facilitate Li ion liberation, render them potential candidates for solid-state Li electrolytes. In contrast, the relatively strong covalent bonding interactions in Zn-based halides may hinder Zn ion migration. Consequently, traditional Zn-based halides with a Zn-halogen structure may not be able to effectively conduct Zn ions, thereby rendering them unsuitable as solid-state Zn-ion electrolytes. This further suggests that the design structure of all-solid electrolytes in Zn batteries cannot be modeled after Li-ion halide solid electrolytes.

To validate the above point, the migration pathways of reported Li-ion solid-state halide electrolyte materials (Li-ion ternary halides)<sup>22–26</sup> and Zn-ion ternary halides were calculated by using a bond valence site energy (BVSE) method<sup>27,28</sup> (Supplementary Data 3). In the case of Li-ion solid electrolytes,  $\beta$ - $Li_2ZrCl_6$  serves as an example, as shown in Fig. 1e. It exhibits a significantly low migration energy barrier for a 2D ionic pathway, at only 0.47 eV, which is consistent with the previously reported study<sup>26</sup>. Supplementary Fig. 8 and Supplementary Table 1 have summarized the typically reported Li-ion solid-state electrolyte halides, which consistently demonstrate a pathway characterized by a relatively low migration energy barrier (0.47–0.57 eV). In contrast, the calculated migration energy barriers for Zn-ion ternary halide material  $Cs_2ZnCl_4$  exceed 1.23 eV (Fig. 1f). As further shown in Supplementary Fig. 9 and Supplementary Table 2, additional calculations suggest that the migration energy barriers of Zn-ion ternary halides (0.96–1.48 eV) are relatively higher than those of previously reported Li-ion solid-state electrolyte halides. These results indicate that the conventional Zn-ion ternary halides may not be suitable for solid-state Zn-ion electrolytes, and it is crucial to mitigate the strong interaction between Zn ions and halide anions. Subsequently, constructing a channel for Zn-ion migration is significant to obtain superior solid-state Zn-ion electrolytes.

We propose a composition engineering strategy that involves replacing the skeleton metal ions in Zn ion ternary halides with organics, aiming to construct potential Zn ion solid electrolytes. Figure 1g illustrates the specific methodology of this composition engineering, wherein the inorganic A-site cations in the original  $A_2ZnX_4$  (A = Cs or Rb; X = halogen) are replaced with organic groups R (R = organic clusters) to form the  $RZnX_4$ . Given that the original inorganic cations are spherical, their spatial positions tend to be relatively compact, making it difficult for these materials to form Zn ion channels. After component engineering design, the target material contains organic cationic groups, which exhibit a comparatively loose spatial configuration. This may facilitate transmission possibilities for Zn ions. In addition, the integration of organic cations may provide more abundant defect properties for materials, thereby enhancing the kinetics of Zn-ion transport. Based on the principle of charge balance, a

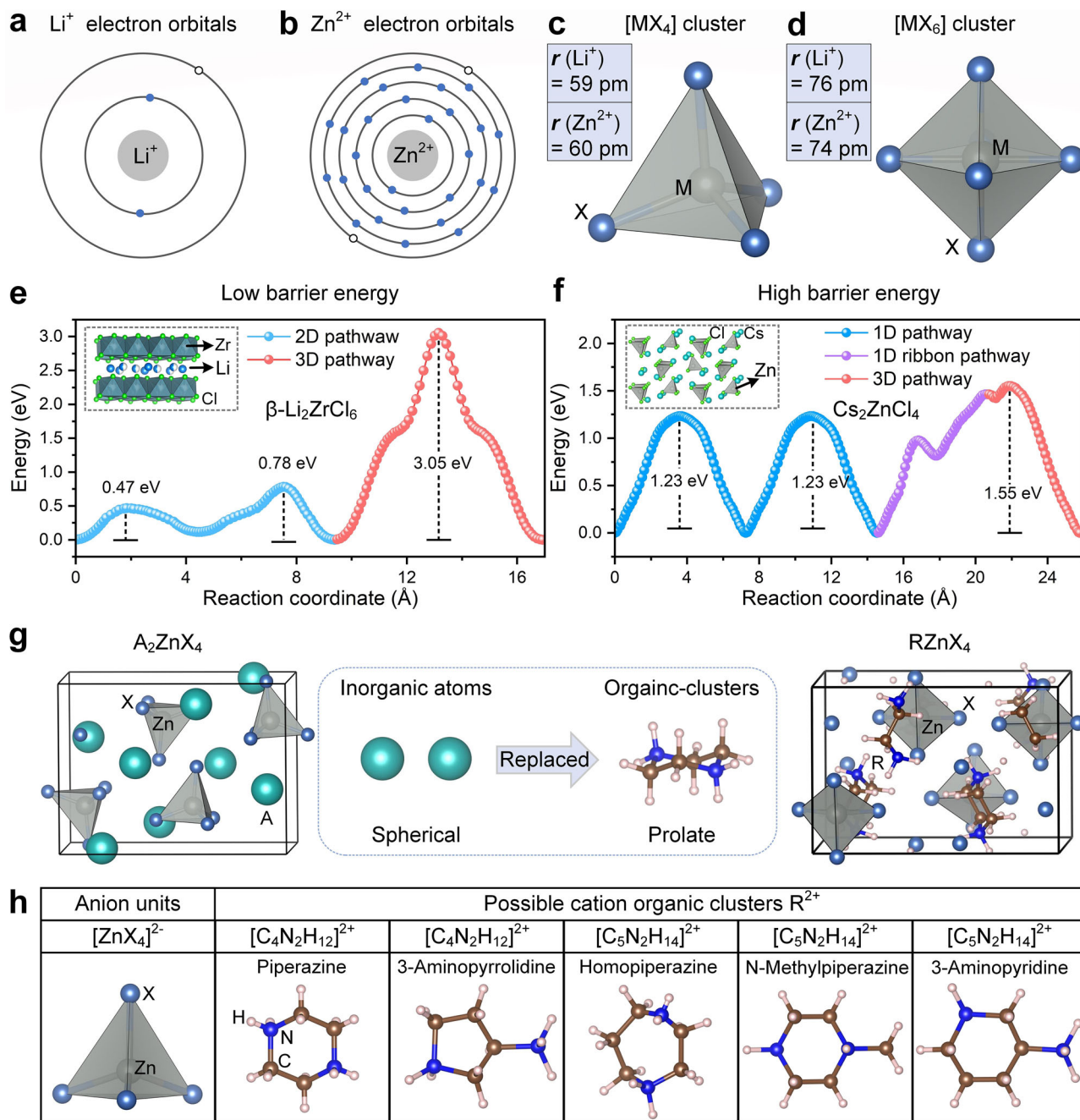


**Fig. 1 | Comparison of properties of Li/Zn-based halide materials and composition engineering design of Zn-ion solid electrolytes. a, b** Electron orbital configurations of  $\text{Li}^+$  and  $\text{Zn}^{2+}$ . Solid blue spheres represent occupied electrons, while orbitals with hollow black spheres represent empty orbitals. **c, d** Metal-halogen tetrahedron  $\text{c}$   $\text{MX}_4$  and octahedron  $\text{d}$   $\text{MX}_6$  ( $\text{M} = \text{Li}$  or  $\text{Zn}$ ;  $\text{X} = \text{Halogen}$  atom). **e, f** Energy profiles of Li or Zn ion migration pathways in **e**  $\beta\text{-Li}_2\text{ZrCl}_6$  and

**f**  $\text{Cs}_2\text{ZnCl}_4$ . The insets are the crystal structures of **e**  $\beta\text{-Li}_2\text{ZrCl}_6$  and **f**  $\text{Cs}_2\text{ZnCl}_4$ . **g** Schematic of composition engineering design of Zn-ion solid electrolytes. In the schematic, A represents an inorganic atom, and R represents organic groups. **h** Structure diagrams of anion unit  $[\text{ZnX}_4]^{2-}$  ( $\text{X} = \text{Halogen}$  atom) and some possible organic cationic clusters.

series of possible cation organic clusters are chosen to combine with the  $[\text{ZnX}_4]^{2-}$  units to form soft Zn-based hybrid metal halides (Fig. 1h). Supplementary Fig. 10 shows the structures of the possible organic molecules and corresponding cation clusters.

### Synthesis, chemical phase diagrams, and electronic structure of Materials

After a series of experimental explorations based on the above strategy, two representative materials, i.e.,  $\text{PipZnBr}_4$  and  $\text{PipZnCl}_4$ , were synthesized through a facile solvothermal reaction. The parent compound halides were prepared by hydrothermal heating of

commercially available zinc bromide ( $\text{ZnBr}_2/\text{ZnCl}_2$ ) and piperazine in hydrobromic acid ( $\text{HBr}/\text{HCl}$ ). The mixture solution was heated to  $90^\circ\text{C}$  within 120 min, and kept for 2440 min, then cooling of the solution yielded soft co-crystalline halides. As shown in Fig. 2a and c, the crystals of both  $\text{PipZnBr}_4$  and  $\text{PipZnCl}_4$  belong to the same space group,  $P2_12_1$  (NO. 19), in the orthorhombic system, which is consistent with the previously reported results<sup>29</sup> and the simulated X-ray diffraction (XRD) patterns from Cambridge Crystallographic Data Centre (CCDC) database (Supplementary Fig. 11). The computation of the chemical phase diagrams can provide additional evidence supporting the stability of these two materials. Given that the organic clusters effectively

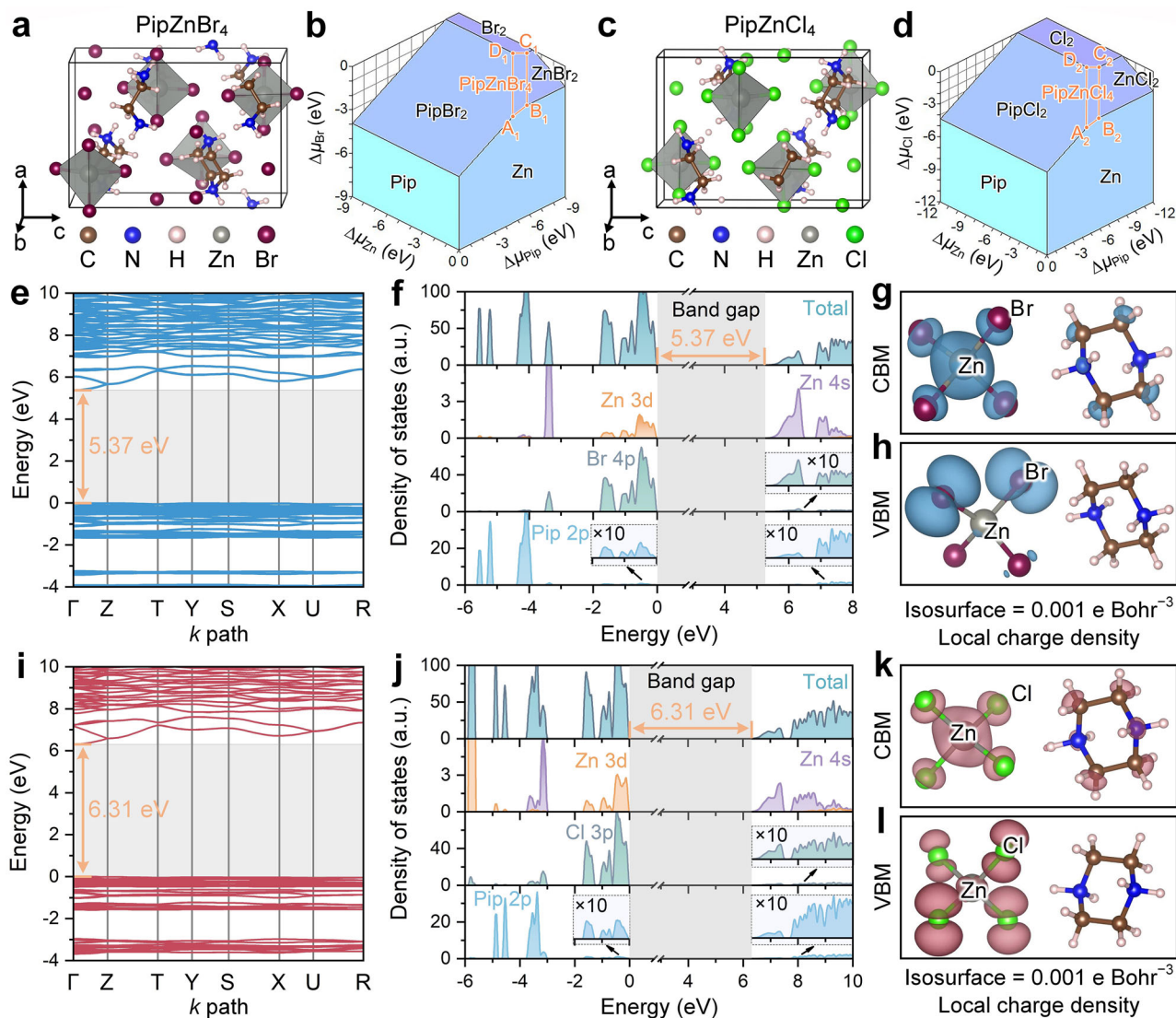


**Fig. 2 | Crystal structures, chemical phase diagrams, and electronic structures of PipZnBr<sub>4</sub> and PipZnCl<sub>4</sub>.** **a, c** Primitive cells of **(a)** PipZnBr<sub>4</sub> and **(c)** PipZnCl<sub>4</sub>. **b, d** Chemical phase diagrams of **(b)** PipZnBr<sub>4</sub> and **(d)** PipZnCl<sub>4</sub>. **e–i** Calculated **(e, i)** band structure, **(f, j)** total and projected DOSs, local charge density at **(g, k)** CBM

and **(h, l)** VBM of PipZnBr<sub>4</sub> and PipZnCl<sub>4</sub>, respectively. The zero in band structures and DOSs is denoted as the VBM. The insets in **(f and j)** represent projected DOSs which have been enlarged by 10 times for clearer indication of their orbital contributions. The isosurfaces of local charge density are all set to 0.001 e Bohr<sup>-3</sup>.

function as a cation in both materials, we consider the whole system as a three-component compound for defect calculations. The chemical phase diagrams of PipZnBr<sub>4</sub> and PipZnCl<sub>4</sub> were determined by the known competing phases in Supplementary Table 3 (Supplementary Data 4). Both PipZnBr<sub>4</sub> and PipZnCl<sub>4</sub> show trapezoidal thermochemical stability windows, indicating their good thermodynamic stability and would be synthesizable. (Fig. 2b and d). The chemical boundary points of PipZnBr<sub>4</sub> are marked as A<sub>1</sub>, B<sub>1</sub>, C<sub>1</sub>, and D<sub>1</sub>, while those of PipZnCl<sub>4</sub> are represented as A<sub>2</sub>, B<sub>2</sub>, C<sub>2</sub>, and D<sub>2</sub>. The calculated chemical potentials, that are,  $\Delta\mu_{\text{Pip}}$ ,  $\Delta\mu_{\text{Zn}}$ ,  $\Delta\mu_{\text{Br}}/\Delta\mu_{\text{Cl}}$ , in the chemical phase diagrams are shown in the Supplementary Tables 4 and 5.

To evaluate the electronic conductivity of PipZnBr<sub>4</sub> and PipZnCl<sub>4</sub> materials, the electronic structures of both materials were investigated systematically. For PipZnBr<sub>4</sub>, the Heyd–Scuseria–Ernzerhof (HSE) calculated band structure shows a large direct band gap of (5.37 eV) at the  $\Gamma$  point as shown in Fig. 2e, implying a poor electrical conductivity. The density of states (DOS) analysis (Fig. 2f) reveals that the valence band maximum (VBM) is dominated by nonbonding states of Br 4p orbitals, whereas the adjacent valence band region consists of antibonding

states from Zn 3d and Br 4p hybridization. The conduction band minimum (CBM) primarily consists of the antibonding states of Zn 4s and Br 4p orbitals, as well as partial p orbitals of organic cations (Fig. 2f). Additionally, the local charge density can provide a more intuitive representation of the orbital contributions to support this interpretation. As shown in Fig. 2g, the local charge density at CBM shows a near tetrahedron cloud around a Zn atom and semi-spindle electric clouds around a Br atom, which intuitively illustrates the antibonding states of the Zn 3s and Br 4p orbitals. The local charge density at VBM is composed solely of spindle-like p orbital electric clouds on the Br atoms (Fig. 2h), corresponding to their non-bonding orbitals. For PipZnCl<sub>4</sub>, the higher electronegativity of Cl relative to Br lowers the energy of Cl 3p orbitals, which results in stronger Zn 4s–Cl 3p orbital hybridization. This effect enhances the splitting between bonding and anti-bonding states, significantly elevating the energy of the anti-bonding orbital at the CBM. Consequently, PipZnCl<sub>4</sub> exhibits a larger band gap (6.31 eV) compared to PipZnBr<sub>4</sub> (5.37 eV), as depicted in Fig. 2i. The DOS and local charge density of PipZnBr<sub>4</sub> are very similar to those of PipZnCl<sub>4</sub>, except that the orbital contribution changes from Br 4p to Cl 3p (Fig. 2j–l). These results imply that both materials exhibit

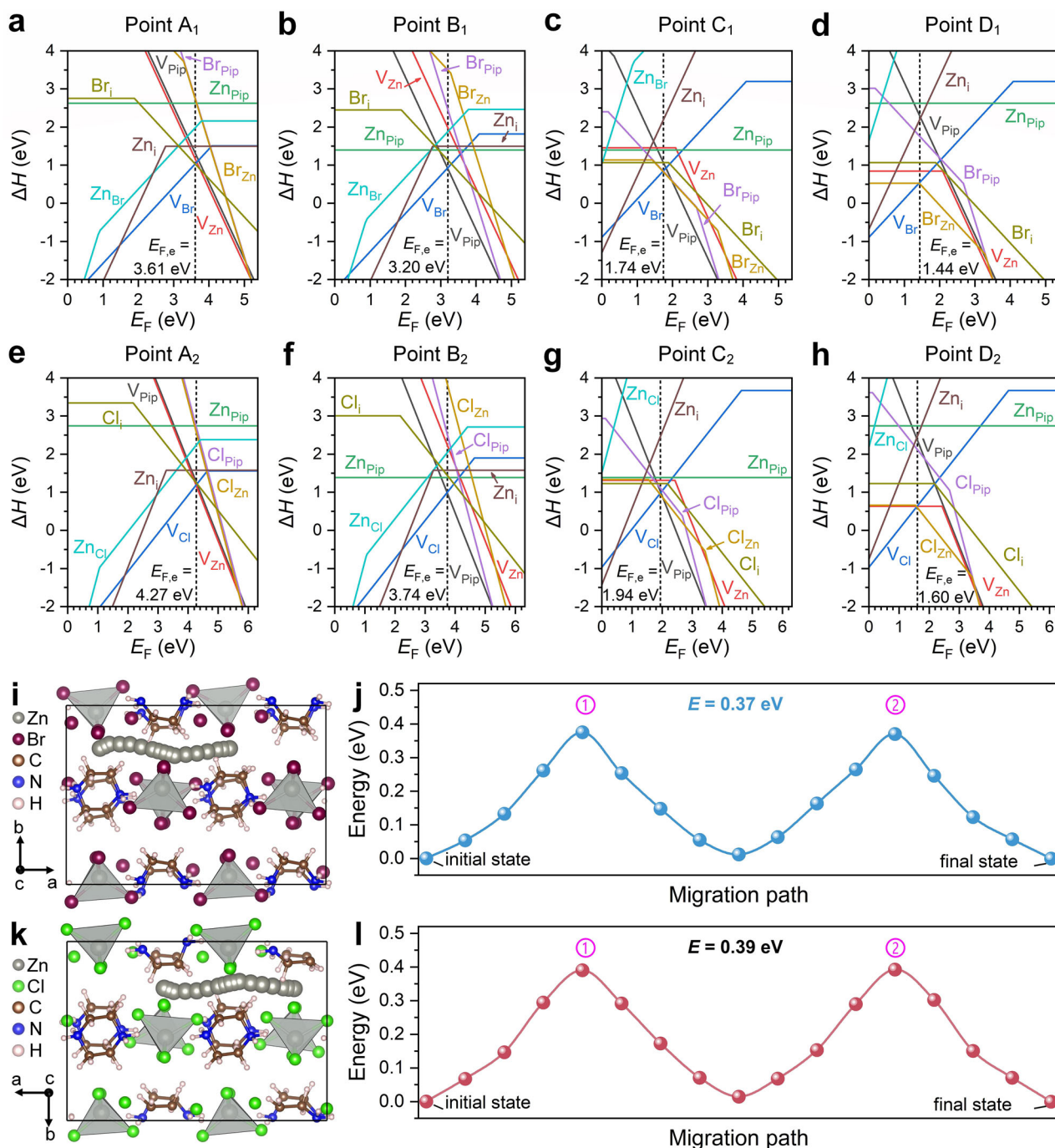


**Fig. 3 | Defect properties and Zn-ion migrations of PipZnBr<sub>4</sub> and PipZnCl<sub>4</sub>.** **a–h** Calculated formation enthalpies ( $\Delta H$ ) of intrinsic defects in **(a–d)** PipZnBr<sub>4</sub> and **(e–h)** PipZnCl<sub>4</sub> as a function of Fermi level ( $E_F$ ) at different chemical potential points: **a** point A<sub>1</sub>, **b** point B<sub>1</sub>, **c** point C<sub>1</sub>, **d** point D<sub>1</sub>, **e** point A<sub>2</sub>, **f** point B<sub>2</sub>, **g** point C<sub>2</sub>, **h** point

D<sub>2</sub>. Defects with very high  $\Delta H$  are not shown in the figures. The calculated equilibrium  $E_F$  ( $E_{F,e}$ ) is denoted by vertical black dash lines. **i**, **k** The Zn-ion migration schematic diagrams along a-axis of **i** PipZnBr<sub>4</sub> and **k** PipZnCl<sub>4</sub>. **j**, **l** The corresponding Zn-ion migration paths of **j** PipZnBr<sub>4</sub> in **(i)** and **l** PipZnCl<sub>4</sub> in **(k)**, respectively.

good stability and a high degree of electronic insulation, thereby suggesting their potential as solid-state Zn-ion electrolytes.

### Defect properties and Zn-ion migration analysis

The defect properties and the Zn-ion migrations of PipZnBr<sub>4</sub> and PipZnCl<sub>4</sub> were calculated to evaluate their potential carrier mobility and ionic conductivity. Because the piperazine cluster is much larger than Zn and Br/Cl atoms, nine intrinsic point defects are considered, i.e., three vacancies ( $V_{\text{Pip}}$ ,  $V_{\text{Zn}}$ , and  $V_{\text{Br/Cl}}$ ), four antisites ( $\text{Br}_{\text{Pip/ClPip}}$ ,  $\text{Br}_{\text{Zn/ClZn}}$ ,  $\text{Zn}_{\text{Pip}}$ , and  $\text{Zn}_{\text{Br/Cl}}$ ), and two interstitials ( $\text{Zn}_i$  and  $\text{Br}_i/\text{Cl}_i$ ) (Supplementary Data 5). The defect models used a  $2 \times 2 \times 2$  supercell

structure (Supplementary Fig. 12). The formation enthalpies ( $\Delta H$ ) of the above-mentioned intrinsic defects as a function of Fermi level ( $E_F$ ) at each boundary point based on Fig. 2b and d are plotted in Fig. 3a–h, and the corresponding transition levels  $\varepsilon(q/q')$  of acceptor-like and donor-like defects are summarized in Supplementary Figs. 13 and 14. Among the calculated nine intrinsic point defects,  $V_{\text{Br/Cl}}$ ,  $\text{Br}_i/\text{Cl}_i$ ,  $V_{\text{Zn}}$ ,  $V_{\text{Pip}}$ , and  $\text{Br}_{\text{Zn/ClZn}}$  are the dominant defects, which determine the electrical properties of PipZnBr<sub>4</sub> and PipZnCl<sub>4</sub>. Under the Zn-rich and Br/Cl-poor condition (Point A<sub>1</sub> and A<sub>2</sub>), the primary donor defect is halogen vacancy ( $V_{\text{Br/Cl}}$ ), while the domain acceptor defects are  $V_{\text{Pip}}$ ,  $V_{\text{Zn}}$ , and  $\text{Br}_i/\text{Cl}_i$ , indicating complex defect chemistry in this condition.

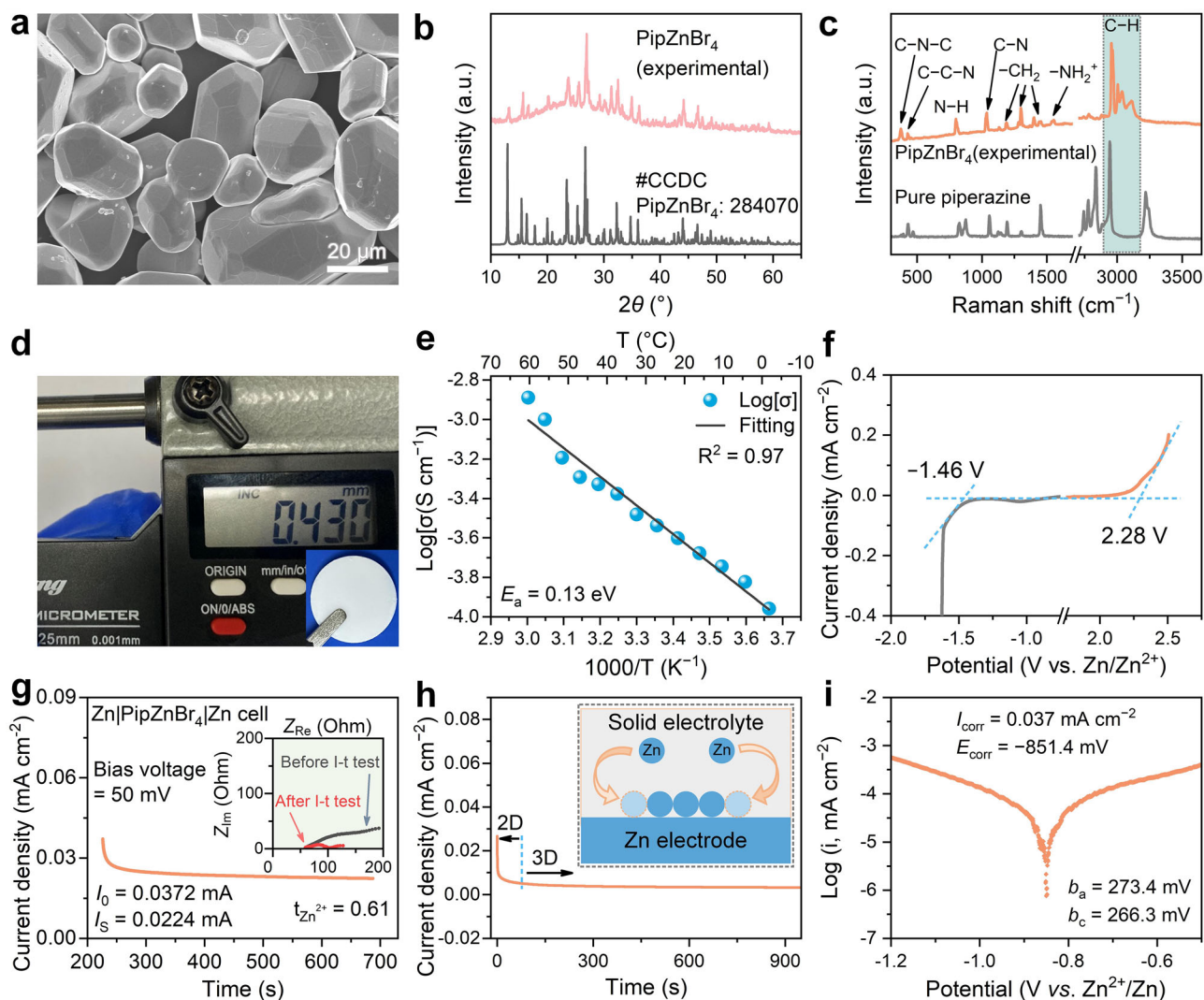


**Fig. 4 | Structural and electrochemical characterizations of the synthesized soft PipZnBr<sub>4</sub> solid-state electrolyte. a** SEM image of pure PipZnBr<sub>4</sub> powder. **b** XRD spectra of PipZnBr<sub>4</sub> powder. **c** Raman spectra of piperazine and PipZnBr<sub>4</sub>. **d** Photograph of PipZnBr<sub>4</sub> electrolyte. **e** Arrhenius plots of PipZnBr<sub>4</sub> as a function of

temperature from 0 to 60 °C. **f** Electrochemical stability window of PipZnBr<sub>4</sub> electrolyte at 1 mV s<sup>-1</sup>. **g** Zn-ion transfer number of PipZnBr<sub>4</sub> electrolyte at 25 °C. **h** CA test of Zn metal at a -100 mV overpotential in PipZnBr<sub>4</sub> electrolyte. **i** Tafel polarization curve in PipZnBr<sub>4</sub> electrolyte.

The equilibrium Fermi levels ( $E_{F,e}$ ) for PipZnBr<sub>4</sub> and PipZnCl<sub>4</sub> at Points A<sub>1</sub>/A<sub>2</sub> are 3.61 eV and 4.27 eV above the VBM, respectively (Fig. 3a and e). As the chemical potential gradually shifts from Br-poor to Br-rich (from point A<sub>1</sub> to D<sub>1</sub>), the  $E_{F,e}$  of PipZnBr<sub>4</sub> moves correspondingly from near the VBM towards the CBM (Fig. 3a–d). Similarly, for PipZnCl<sub>4</sub>, as the chemical potential changes from Cl-poor to Cl-rich (from point A<sub>2</sub> to D<sub>2</sub>), its  $E_{F,e}$  also has a similar shift trend (Fig. 3e–h). Crucially, no matter how the  $E_{F,e}$  of PipZnBr<sub>4</sub> and PipZnCl<sub>4</sub> changes, it is far away from the band edge, and the corresponding hole density ( $N_h$ ) or electron density ( $N_e$ ) is very low (Supplementary Tables 6 and 7). These results further show the electronically insulating nature of these two materials. It should be noted that the dominant donor defects are always the halogen vacancy defects ( $V_{Br}$  for PipZnBr<sub>4</sub> and  $V_{Cl}$  for PipZnCl<sub>4</sub>), while the dominant acceptor defects change with different chemical potential. The dominant halogen vacancy defects suggest that both materials are susceptible to breaking the original Zn-halogen tetrahedral structure due to these defects, which may provide more space for Zn ion conduction.

To evaluate the Zn-ion mobility in PipZnBr<sub>4</sub> and PipZnCl<sub>4</sub>, the Zn ion pathways for a Zn atom confined with two materials were investigated by the climbing image nudged elastic band (CI-NEB) method<sup>30</sup>

(Supplementary Data 6). Exploration of migration pathways along all three axis directions revealed that the lowest energy barriers occur along the a-direction (Fig. 3i–l and Supplementary Figs. 15 and 16). As shown in Fig. 3i and k, the migration of the Zn-ion along the a-axis occurs almost in the direction of the calculated supercells, specifically through the gap between the  $[ZnX_4]^{2-}$  units and the organic cations. The corresponding energy barriers for Zn ion diffusion along the a-direction in PipZnBr<sub>4</sub> and PipZnCl<sub>4</sub> are 0.37 eV (Fig. 3j) and 0.39 eV (Fig. 3l), respectively, which means Zn ions can easily migrate in the two materials. The migration results of Zn-ion in PipZnBr<sub>4</sub> and PipZnCl<sub>4</sub> indicate that both materials exhibit good Zn-ion conductivity. The above defect properties and the Zn-ion migration calculation results suggest that both materials have good electronically insulating properties and Zn-ion conductivity, which shows great potential as superior solid-state Zn-ion electrolytes.

### Structural and electrochemical characterization of hybrid Zn halides

Based on the above theoretical calculation guidance, we use PipZnBr<sub>4</sub> as a case study to further explore the practical application of Zn-ion electrolytes. Defect regulation was achieved by adding excess ZnBr<sub>2</sub>

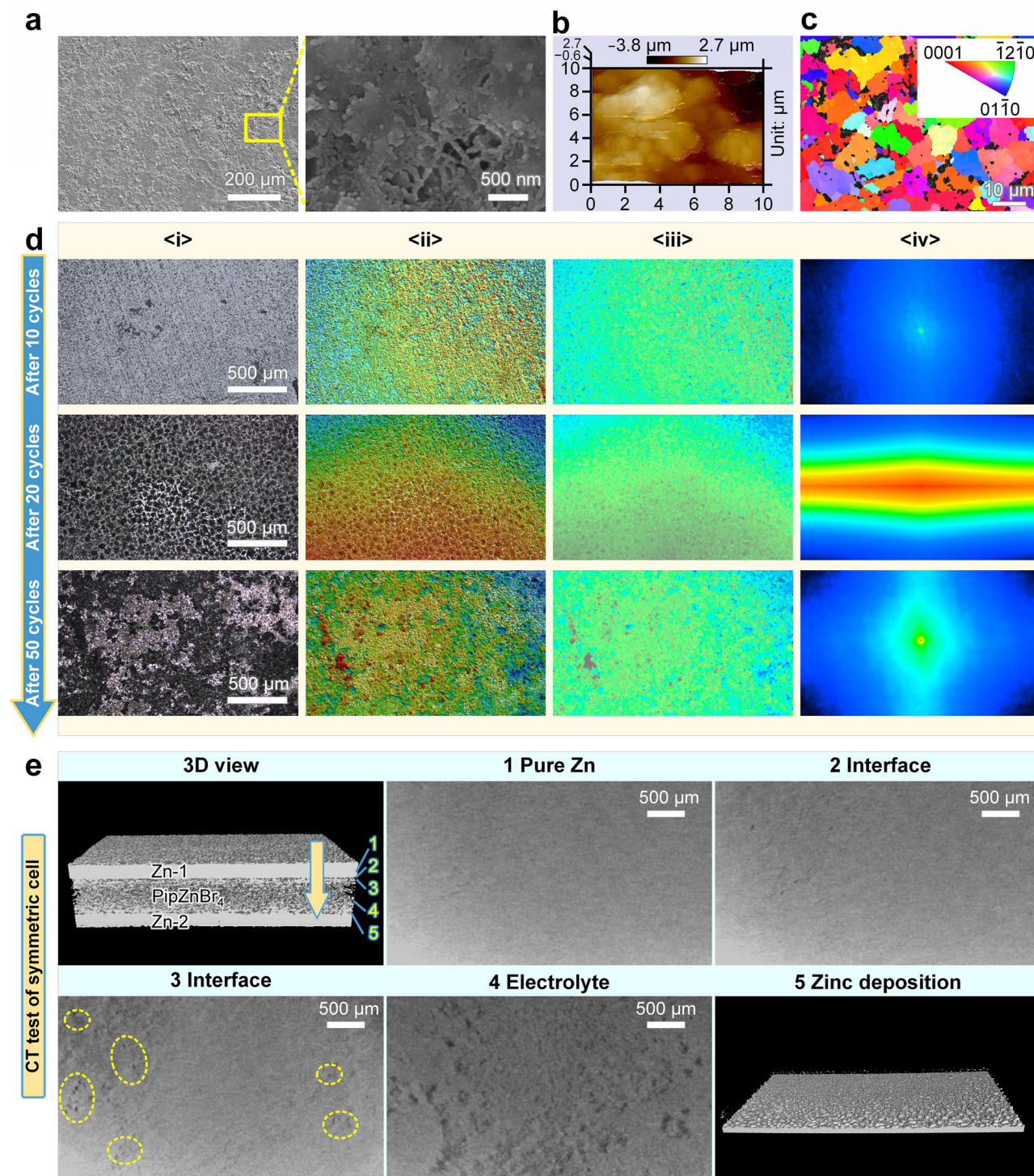


**Fig. 5 | Zn deposition behavior of PipZnBr<sub>4</sub> solid-state electrolyte.** **a** SEM images of Zn deposition on Zn foil after 20 cycles at  $0.1 \text{ mA cm}^{-2}$  and  $0.1 \text{ mAh cm}^{-2}$  in PipZnBr<sub>4</sub> electrolyte. **b** AFM topography image of Zn negative electrode surface in PipZnBr<sub>4</sub> electrolyte following 20 cycles at  $0.1 \text{ mA cm}^{-2}$  and  $0.1 \text{ mAh cm}^{-2}$ . **c** EBSD inverse pole mapping of Zn foil surface after 20 cycles. **d** 3D CLSM images and

correlation function of Zn negative electrode surfaces in PipZnBr<sub>4</sub> electrolyte after different cycles at  $0.1 \text{ mA cm}^{-2}$  and  $0.1 \text{ mAh cm}^{-2}$ . <i> Confocal optical morphology, <ii> contour rough structure, <iii> meter surface area, and <iv> analogs irradiation correlation function on Zn electrode. **e** CT of a Zn symmetric cell tested in PipZnBr<sub>4</sub> electrolyte after 20 cycles at  $0.1 \text{ mA cm}^{-2}$  and  $0.1 \text{ mAh cm}^{-2}$ .

compared to piperazine to increase the ionic conduction. Specifically, the feed molar ratio of piperazine to ZnBr<sub>2</sub> was regulated from 1:1 to 1:5, corresponding denoted as PipZnBr<sub>4</sub> (1:1) and PipZnBr<sub>4</sub>. As characterized by scanning electron microscopy (SEM) in Fig. 4a and Supplementary Fig. 17, PipZnBr<sub>4</sub> shows irregular polygonal particles with a diameter of 10–80 μm. The XRD analysis of the prepared hybrid Zn halides was implemented to verify the crystal structure. As shown in

Fig. 4b and Supplementary Fig. 18a, the experimentally obtained powder XRD patterns of PipZnBr<sub>4</sub> correspond well with the simulated pattern (# CCDC PipZnBr<sub>4</sub>: 284070), especially PipZnBr<sub>4</sub> (1:1), indicating excess ZnBr<sub>2</sub> does not affect the crystal structure of compound PipZnBr<sub>4</sub><sup>29</sup>. The chemical structures of the as-synthesized PipZnBr<sub>4</sub> sample were studied by Raman spectroscopy and Fourier transform infrared (FTIR) tests. As shown in Fig. 4c, compared with pure

piperazine, the PipZnBr<sub>4</sub> exhibits an N–H single peak ( $\sim 816\text{ cm}^{-1}$ ) and a new peak of  $-\text{NH}_2^+$  ( $\sim 1540\text{ cm}^{-1}$ ), manifesting the formation of piperazine ions<sup>31</sup>. The inversion symmetry of C–H bond peaks ( $2700\text{--}3200\text{ cm}^{-1}$ ) also illustrates the formation of the compound PipZnBr<sub>4</sub><sup>32</sup>. The Raman peak of the prepared PipZnBr<sub>4</sub> (1:1) has a similar situation (Supplementary Fig. 18b). Additionally, the presence of  $-\text{NH}_2^+$  peak in FTIR spectra of PipZnBr<sub>4</sub> and PipZnBr<sub>4</sub> (1:1) verifies the formation of the soft PipZnBr<sub>4</sub> (Supplementary Fig. 19). Significantly, the FTIR spectra also show that the addition of excess ZnBr<sub>2</sub> does not impact the structure of the compound PipZnBr<sub>4</sub>. The Zn content (12.73 wt%) of the synthesized PipZnBr<sub>4</sub> sample with excess ZnBr<sub>2</sub> is only slightly increased compared to the PipZnBr<sub>4</sub> (1:1) (11.99 wt%) by inductively coupled plasma (ICP) measurements (Supplementary Fig. 20), implying that it only exists a small number of vacancies to accelerate ion migration<sup>12</sup>. Additionally, the weight and XRD of PipZnBr<sub>4</sub> remain almost unchanged when the temperature rises to 150 °C in the thermal gravimetric test (Supplementary Fig. 21). Even when the temperature increases to 300 °C, the weight of the sample can remain at 96.5 wt%, indicating the good thermal stability of PipZnBr<sub>4</sub>.

The synthesized PipZnBr<sub>4</sub> sample with excess ZnBr<sub>2</sub> was pressed into a 16 mm diameter pellet with a thickness of  $\sim 430\text{ }\mu\text{m}$  as a solid-state Zn-ion electrolyte for ZMBs (Fig. 4d). The ionic conductivity ( $\sigma$ ) of the pressed pellet of PipZnBr<sub>4</sub> was investigated at different temperatures with 5 °C intervals by electrochemical impedance spectroscopy (EIS) test. The  $\sigma$  value can be calculated according to the total resistance determined by the intercept on the real axis based on fitting Nyquist plots (Supplementary Fig. 22a–m). The temperature-dependent ionic conductivities of PipZnBr<sub>4</sub>, within the range of 0–60 °C, are depicted in Supplementary Fig. 22n. The elevated ion conductivity indicates that PipZnBr<sub>4</sub> serves as a good Zn-ion conductor, aligning with prior computational predictions. Notably, the high  $\sigma$  values of 2.9 and  $4.7 \times 10^{-4}\text{ S cm}^{-1}$  at 25 °C and 40 °C were observed for the PipZnBr<sub>4</sub> pellet, indicating its potential suitability as an all-solid-state Zn-ion electrolyte. Its Arrhenius curve is plotted in Fig. 4e to calculate the activation energy ( $E_a$ ) of PipZnBr<sub>4</sub> electrolyte based on the Arrhenius equation. The result shows that PipZnBr<sub>4</sub> has a small activation energy (0.13 eV), indicating its promising application in all-solid-state ZMBs. To verify the high ionic conductivity of PipZnBr<sub>4</sub>, the ionic conductivity of ZnBr<sub>2</sub> has been assessed at 25 °C (Supplementary Fig. 23). Meanwhile, PipZnBr<sub>4</sub> also exhibits a potential range from  $-1.46$  to  $2.28\text{ V}$  (Fig. 4f), which is much wider than the electrochemical window of 1.2 M zinc trifluoromethanesulfonate (Zn(OTf)<sub>2</sub>) aqueous electrolyte (2.02 V)<sup>33</sup> and hydrogel electrolyte (2.13 V)<sup>34</sup>. More significantly, PipZnBr<sub>4</sub> as an all-solid-state Zn-ion electrolyte can display a Zn-ion transfer number ( $t_{\text{Zn}^{2+}}$ ) of 0.61 (Fig. 4g), which effectively regulates Zn-ion flux. While this value suggests contributions from additional ionic migration pathways (e.g., Br<sup>−</sup> ions) in PipZnBr<sub>4</sub> electrolytes, Zn-ion transport remains the dominant mechanism and the Zn-ion transfer number is comparable to that of other solid Zn-ion conductors<sup>35–37</sup>. To investigate the electrochemical process of the Zn electrode, chronoamperometry (CA) tests and voltage-time curves were evaluated. The current density of the PipZnBr<sub>4</sub> electrolyte rises instantaneously and then quickly remains stable (Fig. 4h), implying a three-dimensional (3D) dominating Zn-ion diffusion. Additionally, the PipZnBr<sub>4</sub>-based Zn||Zn solid-state cell shows low initial nucleation overpotentials at 0.1, 0.5, and 1.0 mA cm<sup>−2</sup> (Supplementary Fig. 24). This phenomenon suggests that Zn ions are prone to be reduced and nucleated at the active sites, resulting in a uniform and dense Zn deposition. To study the anti-corrosion property of PipZnBr<sub>4</sub>, the tafel polarization curve was tested (Fig. 4i). The Zn electrode in the PipZnBr<sub>4</sub> electrolyte delivers a lower corrosion potential ( $E_{\text{corr}} = -851.4\text{ mV}$  vs. Zn<sup>2+</sup>/Zn) and a much lower corrosion current density ( $I_{\text{corr}} = 0.037\text{ }\mu\text{A cm}^{-2}$ ) than a 1.2 M Zn(OTf)<sub>2</sub> aqueous solution<sup>33</sup>, implying the weak adverse reaction.

## Zn deposition behavior

The impact of PipZnBr<sub>4</sub> electrolyte on the Zn deposition behavior was first observed by SEM. As shown in Fig. 5a and Supplementary Fig. 25, the uniform and compact spherical deposition of Zn is exhibited in PipZnBr<sub>4</sub> Zn-ion electrolyte after 20 cycles at 0.1 mA cm<sup>−2</sup> and 0.1 mAh cm<sup>−2</sup>, suggesting good Zn deposition behavior. The spherical morphology and Young's modulus of the Zn electrode after different cycles were further characterized by atomic force microscopy (AFM). The mean modulus value and average height of the Zn negative electrode following 20 cycles are 2.1 GPa and 0.9  $\mu\text{m}$  (Fig. 5b), while the Zn foil after 50 cycles at 0.1 mA cm<sup>−2</sup> and 0.1 mAh cm<sup>−2</sup> shows a slightly larger modulus value (3.6 GPa) and average height (2.3  $\mu\text{m}$ ) (Supplementary Fig. 26). These results illustrate that the PipZnBr<sub>4</sub> electrolyte induces a deposition behavior of densely compacted Zn grains. To characterize the Zn crystal orientation and crystal structure regularity, electron backscatter diffraction (EBSD) was implemented<sup>38</sup>. As shown in Fig. 5c, the Zn grains from Zn foil in the PipZnBr<sub>4</sub> electrolyte after 20 cycles at 0.1 mA cm<sup>−2</sup> and 0.1 mAh cm<sup>−2</sup> exhibit irregularity, and the grain boundaries are interlaced, implying polycrystalline and random orientation characteristics<sup>39</sup> (Supplementary Fig. 27). From the ex situ 3D confocal laser scanning microscopy (CLSM), the Zn negative electrodes in PipZnBr<sub>4</sub> electrolyte after different cycles at 0.1 mA cm<sup>−2</sup> and 0.1 mAh cm<sup>−2</sup> also present uniform and compact Zn grain deposition (Fig. 5di–iii), which is consistent with the AFM results. The Zn negative electrode surface after 10 cycles at 0.1 mA cm<sup>−2</sup> shows a larger surface roughness (2.8  $\mu\text{m}$ ), higher surface volume ( $1.9 \times 10^7\text{ }\mu\text{m}^3$ ), and larger surface area ( $4.6 \times 10^6\text{ }\mu\text{m}^2$ ) than those of the Zn negative electrode after 30 and 50 cycles (Supplementary Fig. 28 and Supplementary Table 8), confirming the notably even Zn deposition with the cycling. By contrast, the surface roughness (4.9  $\mu\text{m}$ ) is the largest for the Zn electrode after 20 cycles at 0.1 mA cm<sup>−2</sup> and 0.1 mAh cm<sup>−2</sup>, which may be because the electrode is slightly less dense in the early deposition. Intuitively, the self-correlation function of the Zn electrode surface roughness after 50 cycles shows the region with an unclear boundary (Fig. 5div) due to the weak self-correlation, indirectly indicating uniform and dense Zn deposition<sup>34</sup>.

To further investigate the internal structure and non-destructive Zn deposition morphology, Computed tomography (CT) technology was implemented for the PipZnBr<sub>4</sub>-based solid-state Zn||Zn cell after 20 cycles at 0.1 mA cm<sup>−2</sup> and 0.1 mAh cm<sup>−2</sup>. The PipZnBr<sub>4</sub>-based battery is divided into five parts to understand details the contact between the Zn electrode and electrolyte (Fig. 5e). Obviously, the CT of the 1-Zn electrode presents a smooth texture (Fig. 5e (1)), which suggests that the Zn foil here is not involved in the electrochemical reaction. Figure 5e (2) presents a uniform and flat interface between the Zn electrode and electrolyte, implying good interface contact. Further closer to the electrolyte, it is found that a small number of uneven pits appear at the interface (Fig. 5e (3)), which may be caused by the solid and particulate PipZnBr<sub>4</sub> electrolyte. As shown in Fig. 5e (4), the CT of the solid electrolyte further verifies the uniform interface. To observe the interfacial contact of the entire battery system, the interface CT was also studied by dynamically recording the CT images of the cross-section of the solid-state Zn symmetrical cell (Supplementary Fig. 29). It is observed that the Zn electrodes and electrolyte maintain close contact after 20 cycles, which contributes to retaining the integrity of the electrolyte and restraining the occurrence of Zn dendrites and other side reactions. Due to the intimate contact at the Zn/PipZnBr<sub>4</sub> electrolyte interface and the good reaction kinetics, the Zn surface exhibits uniform and compact Zn spherical deposition (Fig. 5e (5)), which is consistent with SEM and AFM results. The PipZnBr<sub>4</sub>-based Zn symmetrical cell was disassembled after the CT test, and then the properties of the electrolyte and the Zn electrodes were investigated. Compared with pure PipZnBr<sub>4</sub> powder (Supplementary Fig. 17), the PipZnBr<sub>4</sub> electrolyte after Zn plating/stripping at 0.1 mA cm<sup>−2</sup> and 0.1 mAh cm<sup>−2</sup> exhibits a smaller particle size (Supplementary Fig. 30), which may be because the high pressure

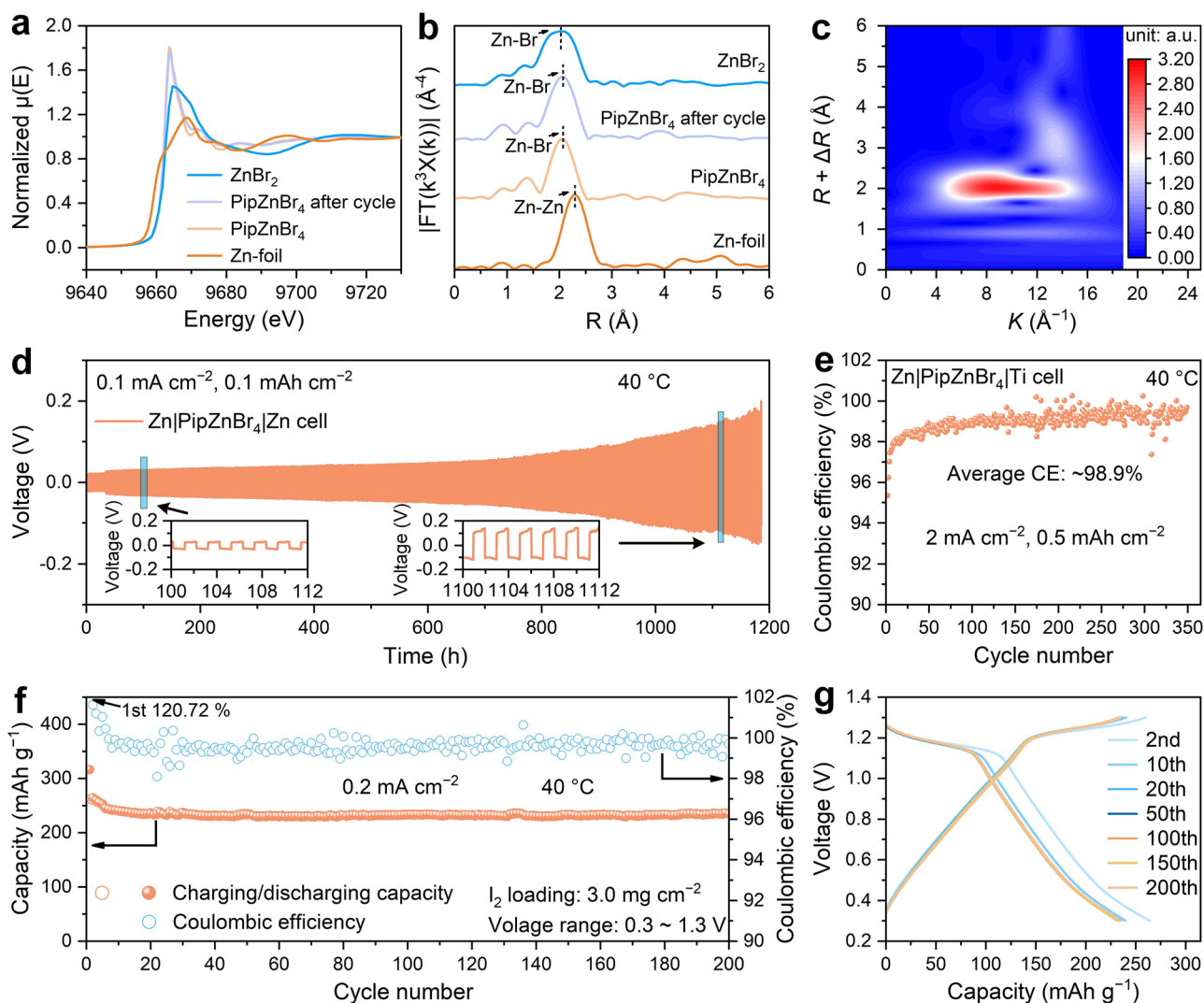


**Fig. 6** | XAFS characterization and electrochemical performance of PipZnBr<sub>4</sub>-based solid-state cells at 40 °C. **a** Normalized Zn *K*-edge XANES spectra. **b** Fourier-transformed EXAFS spectra in *R* space. **c** Wavelet-transformed *k*<sup>3</sup>-weighted Zn *K*-edge EXAFS spectrum of PipZnBr<sub>4</sub> after 20 cycles. **d** Long cycle stability of a Zn||Zn

cell with PipZnBr<sub>4</sub> electrolyte at 0.1 mA cm<sup>-2</sup> with 0.1 mAh cm<sup>-2</sup>. **e** CE measurements of a Zn||Ti cell at 2.0 mA cm<sup>-2</sup> and plating capacity of 0.5 mAh cm<sup>-2</sup> in PipZnBr<sub>4</sub> electrolyte. **f** Stable Zn plating/stripping performance of a Zn||PipZnBr<sub>4</sub>||I<sub>2</sub> full cell at 0.2 mA cm<sup>-2</sup>. **g** Corresponding GCD curves of a Zn||I<sub>2</sub> cell.

used in the preparation of the all-solid-state Zn-ion electrolyte pellet causes the PipZnBr<sub>4</sub> powder to crush. The XRD spectra of the electrolyte after Zn plating/stripping do not change significantly compared to pure PipZnBr<sub>4</sub> powder (Supplementary Fig. 31). After 20 cycles at 0.1 mA cm<sup>-2</sup> and 0.1 mAh cm<sup>-2</sup>, the peak positions of C 1s, N 1s, Br 3d, Zn LMM, and Zn 2p X-ray photoelectron spectroscopy (XPS) shift to a high energy level as a whole (Supplementary Fig. 32). This may be caused by the application of voltage to the cell during Zn plating/stripping, inducing environment change of the elements in the PipZnBr<sub>4</sub> electrolyte, implying that the PipZnBr<sub>4</sub> has good structural stability. Additionally, the surface composition of the Zn electrode after 20 cycles was characterized. Compared with the bare Zn foil, the electrode surface after Zn plating/stripping at 0.1 mA cm<sup>-2</sup> and 0.1 mAh cm<sup>-2</sup> shows some new peaks (Supplementary Fig. 33). The XPS test with Ar<sup>+</sup> sputtering was further used to measure the interphase chemistry on the Zn electrode surface in all-solid-state Zn-ion electrolyte after 20 cycles at 0.1 mA cm<sup>-2</sup> and 0.1 mAh cm<sup>-2</sup> (Supplementary Fig. 34). It is found that the in situ formed solid electrolyte interphase (SEI) layer on Zn surface features an organic-rich outer layer and an inorganic-rich inner layer, which contributes to suppressing dendrite formation and promoting Zn-ion diffusion<sup>40</sup>.

### Characterizations and electrochemical performance of PipZnBr<sub>4</sub>-based solid Zn batteries

To explore the change of element valence state in the PipZnBr<sub>4</sub> electrolyte and its stability before and after Zn plating/stripping at 0.1 mA cm<sup>-2</sup> and 0.1 mAh cm<sup>-2</sup>, X-ray absorption fine structure (XAFS) tests were executed. Figure 6a shows the normalized X-ray absorption near-edge structure (XANES) spectra at Zn *K*-edge for pure ZnBr<sub>2</sub>, Zn-foil, pure PipZnBr<sub>4</sub>, and PipZnBr<sub>4</sub> after 20 cycles. Obviously, the Zn-foil demonstrates the lowest edge absorption energy in XANES, a characteristic primarily attributable to the inherent zero-valence state of the Zn-foil<sup>41</sup>. By contrast, the absorption edges of the remaining materials are essentially identical, suggesting the divalent of Zn in them. The Fourier transform spectra of the extended XAFS (EXAFS) curves in *R*-space show that the bond length of Zn–Br in PipZnBr<sub>4</sub> is longer than that in pure ZnBr<sub>2</sub> (Fig. 6b), which suggests a relatively weaker Zn–Br bond in PipZnBr<sub>4</sub>. Additionally, the results of the XANES (Fig. 6a), Fourier-transformed EXAFS (Fig. 6b), and the wavelet-transformed *k*<sup>3</sup>-weighted Zn *K*-edge EXAFS spectra (Fig. 6c and Supplementary Fig. 35) of PipZnBr<sub>4</sub> suggest that the Zn–Br bond length remains unchanged before and after Zn plating/stripping at 0.1 mA cm<sup>-2</sup> and 0.1 mAh cm<sup>-2</sup>. This implies

that PipZnBr<sub>4</sub> as a solid-state electrolyte exhibits robust electrochemical stability.

To further assess the interfacial and electrochemical stability of the Zn/PipZnBr<sub>4</sub>, Zn solid-state cells with a PipZnBr<sub>4</sub> electrolyte were investigated systematically. Figure 6d shows the cycling performance of the Zn symmetric cell for over 1100 h at 0.1 mA cm<sup>-2</sup>. The corresponding polarization potential increases gradually with the increase of the Zn plating/stripping time, attributing to the high specific kinetic obstacle and the slow Zn plating/stripping<sup>42</sup>. When the current density is increased to 0.5 mA cm<sup>-2</sup>, the PipZnBr<sub>4</sub>-based Zn symmetric cell still works over 400 h (Supplementary Fig. 36a), implying the stable ionic migration. At an increased current density of 1.0 mA cm<sup>-2</sup>, long Zn plating/stripping process with voltage hysteresis (~860 mV) can still be attained in the symmetric Zn cell (Supplementary Fig. 36b–d). Meanwhile, the cycling stability of Zn||Zn cell using com ZnBr<sub>2</sub> as a solid-state electrolyte was also tested at 0.1 mA cm<sup>-2</sup>. As shown in Supplementary Fig. 37, the short cycle life and large voltage polarization were delivered, suggesting poor ionic conduction. To understand the reversibility of the Zn<sup>2+</sup> plating/stripping process, Zn|PipZnBr<sub>4</sub>|Ti asymmetric cells were tested. Supplementary Figs. 38 and 39 show the rate cyclic voltammetry (CV) curves of the Zn||Ti cell at 25 °C. The extracted curves suggest that reduction potential decreases ( $\Delta V = 70$  mV) as the scanning rate increases (Supplementary Fig. 39), implying the weak parasitic reaction at the Zn/PipZnBr<sub>4</sub> interface, which is different from the continuous reduction potential increase of 2 M ZnSO<sub>4</sub> aqueous electrolyte<sup>43–45</sup>. Figure 6e exhibits the long-term cycle performance of a Zn||Ti cell with PipZnBr<sub>4</sub> solid-state electrolyte. It is found that the cell yields a stable and high average CE of 98.9% at 2 mA cm<sup>-2</sup> and 0.5 mA cm<sup>-2</sup> after 350 cycles associated with the close contact at the Zn/PipZnBr<sub>4</sub> interface. The corresponding voltage profiles at different cycles are presented in Supplementary Fig. 40, and deliver a lower voltage hysteresis (~170 mV) than that of the Zn||Ti cell (~184 mV) with 1 M ZnSO<sub>4</sub> electrolyte due to inhibition of side reaction<sup>33</sup>. As the cutoff capacity is further increased to 1.0 mAh cm<sup>-2</sup>, the Zn||Ti cell still realizes a long lifespan over 115 cycles with an average CE of ~99.6% (Supplementary Fig. 41a), and the corresponding voltage profiles are shown in Supplementary Fig. 41b. These prospective results provide support for using PipZnBr<sub>4</sub> as a solid-state electrolyte in highly reversible ZMBs.

To evaluate the feasibility of PipZnBr<sub>4</sub> electrolyte in practical applications, a Zn|PipZnBr<sub>4</sub>|iodine (I<sub>2</sub>) full all-solid-state Zn-metal battery was assembled, in which I<sub>2</sub> is adopted as a positive electrode and the mass of I<sub>2</sub> loading is ~3 mg cm<sup>-2</sup>. Figure 6f shows the long-term cycle performance of the Zn||I<sub>2</sub> cell. A residual capacity of 234.5 mAh g<sup>-1</sup> and a low capacity degradation rate of 0.056% per cycle is achieved after 200 cycles at 0.2 mA cm<sup>-2</sup>. The corresponding galvanostatic charge/discharge (GCD) curves were observed and found that these curves exhibit good overlap, except for the second cycle (Fig. 6g), implying the high reversibility of Zn<sup>2+</sup> in PipZnBr<sub>4</sub> solid-state electrolyte. Supplementary Fig. 42 illustrates the CV curves at 0.1 and 0.2 mV s<sup>-1</sup> of full cells with distinct iodine-related redox peaks, which exhibit a diminished voltage gap between the cathodic and anodic peaks, indicating an improvement in reaction kinetics. This phenomenon is also corroborated by EIS analysis, which demonstrates reduced charge transfer resistance (Supplementary Fig. 43). When the current density is increased to 0.5 mA cm<sup>-2</sup>, the Zn|PipZnBr<sub>4</sub>|I<sub>2</sub> cell can still operate 100 cycles after the pre-activation process at the current density of 0.5 mA cm<sup>-2</sup> for 3 cycles (Supplementary Fig. 44a) and corresponding GCD curves are exhibited in Supplementary Fig. 44b. These good performances are attributed to the uniform Zn plating/stripping at the Zn/PipZnBr<sub>4</sub> interface due to the close contact of the interface, inducing homogeneous Zn<sup>2+</sup> flux. Additionally, the FTIR and XPS spectra of the I<sub>2</sub> positive electrode were also tested to exclude the possibility of halogen ion conductivity. Compared with the pristine I<sub>2</sub> electrode, the cycled I<sub>2</sub> positive electrode exhibits no additional peaks

(Supplementary Fig. 45), particularly in the wavenumber ranges of 520–600 cm<sup>-1</sup> and 1300–1500 cm<sup>-1</sup>, where peaks associated with the Br element would typically appear. XPS spectra test with Ar<sup>+</sup> sputtering was also used to assess the chemical component on the I<sub>2</sub> positive electrode surface, when the Zn|PipZnBr<sub>4</sub>|I<sub>2</sub> full cell has undergone 10 cycles at 0.2 mA cm<sup>-2</sup> and then is discharged to 1.0 V (Supplementary Fig. 46). More significantly, as shown in Supplementary Fig. 47, PipZnCl<sub>4</sub> as electrolyte was also evaluated in a Zn symmetric cell and a Zn||I<sub>2</sub> full cell. Finally, to exclude the possibility of halide ion conduction, CsSnBr<sub>3</sub> and CsSnCl<sub>3</sub> samples as the blocking layer were applied in the solid-state PipZnBr<sub>4</sub> and PipZnCl<sub>4</sub> electrolytes (Supplementary Fig. 48). It is found that the CV curves of Zn|PipZnCl<sub>4</sub>|CsSnCl<sub>3</sub>|I<sub>2</sub> and Zn|PipZnCl<sub>4</sub>|CsSnCl<sub>3</sub>|I<sub>2</sub> full cells at 0.1 mV s<sup>-1</sup> have no oxidation-reduction peak and Zn||Zn symmetrical cells at 0.1 mA cm<sup>-2</sup> and 0.1 mAh cm<sup>-2</sup> are almost unable to operate (Supplementary Fig. 49). These results demonstrate that although halide ions could migrate in PipZnBr<sub>4</sub> and PipZnCl<sub>4</sub> electrolytes, Zn-ion conduction in the halide-based ZMBs play a dominant contribution.

## Discussion

In summary, a simple and effective composition engineering strategy for constructing halide Zn-ion electrolytes was proposed based on the theoretical prediction, aiming to obtain good all-solid-state Zn-ion electrolyte materials with low ionic migration barriers. Two typical metal halide materials were obtained, i.e., PipZnBr<sub>4</sub> and PipZnCl<sub>4</sub>. The chemical phase diagram indicates that both materials are thermodynamically stable. The electronic structure of these materials demonstrates an electronically insulating nature and Zn-halogen octahedra dominates their electronic properties. Defect properties and Zn ion migration analysis indicate that these two materials show good prone to have halogen vacancies, and have a low Zn ion migration barrier between the tetrahedra and organic clusters. Theoretical analysis shows that they have the potential to be new solid-state zinc-ion electrolytes. Based on theoretical guidance, PipZnBr<sub>4</sub> was prepared and taken as an example for the application of all-solid-state Zn-ion electrolytes. PipZnBr<sub>4</sub> has a high ionic conductivity ( $2.3 \times 10^{-4}$  S cm<sup>-1</sup> at 25 °C), low activation energy (0.13 eV), wide electrochemical window (~3.74 V vs. Zn<sup>2+</sup>/Zn), and high Zn-ion transfer number (0.61). Significantly, PipZnBr<sub>4</sub> can maintain compact contact with the Zn interface and derive an organic-inorganic SEI layer at the Zn electrode surface during the Zn plating/stripping process, which decreases the interface resistance and promotes the dense Zn spherical deposition. Benefiting from the above advantages of PipZnBr<sub>4</sub>, promising electrochemical performance of a Zn||I<sub>2</sub> cell using PipZnBr<sub>4</sub> as an all-solid-state electrolyte is achieved. This study commences with the robust interaction of Zn halides and constructively introduces a class of hybrid Zn metal halide materials. The feasibility of these materials as Zn-based hybrid metal halide electrolytes is confirmed through both theoretical and experimental methodologies. The investigation into Zn-based hybrid metal halide electrolytes has paved a way for further research in this field.

## Methods

### Orbital analysis and interaction diagram

The orbital analysis of tetrahedral and octahedral structures was performed with the Gaussian16 package<sup>46</sup>. The Becke 3-parameter Lee–Yang–Parr (B3LYP)<sup>47</sup> correlation functional at def2-TZVP<sup>48</sup> level was used for the optimization and self-consistent field calculations, with density functional theory-D3 (Becke-Johnson)<sup>49,50</sup> method for the van der Waals interactions. The visualization of the orbital results was conducted using Multiwfn<sup>51</sup> and Visual Molecular Dynamics<sup>52</sup> software. The irreducible representations, such as  $a_1$ ,  $a_{1g}$ ,  $t_{1g}$ ,  $e_g$ , were also obtained from the Gaussian 16 calculation results. The bonding interactions illustrated in the interaction diagrams were deduced based on

the orbital symmetry information and the spatial distribution/overlap characteristics of the visualized orbitals.

### COBI analysis

The structural models of 4-coordinated/6-coordinated LiCl sourced from the Materials Project database<sup>53</sup>. The optimization calculations of the structures were performed using the projector-augmented wave<sup>54</sup> method, as incorporated in the Vienna Ab initio Simulation Package (VASP)<sup>55</sup> code. The cutoff energy was set to 500 eV.  $\Gamma$ -centered  $k$ -meshes, with a  $k$ -spacing of  $0.2 \text{ \AA}^{-1}$ , were employed for the sampling of the Brillouin zones. The generalized gradient approximation (GGA) Perdew-Burke-Ernzerhof (PBE)<sup>56</sup> was used as the exchange-correlation functional. The energy convergence criterion for COBI analysis is  $10^{-7}$  eV. The COBI values were calculated by using the Lobster<sup>57</sup> code.

### BVSE calculations

BVSE calculations were conducted utilizing the softBV<sup>27,28</sup> software, employing structural models sourced from the Inorganic Crystal Structure Database. The energies of Li or Zn sites within structures were calculated on a three-dimensional grid of points, each with a resolution of  $0.1 \text{ \AA}$ . The pathways of  $\text{Li}^+$  or  $\text{Zn}^{2+}$  migration were automatically obtained by the software.

### Density functional theory (DFT) calculations for electronic structures

DFT calculations were performed using the VASP<sup>55</sup> code. The cut-off energy,  $k$ -points, and exchange-correlation functional settings for all the structures (PipZnBr<sub>4</sub>, PipZnCl<sub>4</sub>, and their possible secondary phases) optimizations were the same as those used in the structure optimization for COBI analysis. The crystal structures of PipZnBr<sub>4</sub> and PipZnCl<sub>4</sub> were fully relaxed until the total force on each atom was  $<0.03 \text{ eV \AA}^{-1}$ . To rectify the underestimation of the band gaps in GGA-PBE methods, the band structure, DOS, and charge density (CBM and VBM) were calculated by using the HSE06<sup>58</sup> hybrid functional. The visualization of the charge density is carried out using the VESTA<sup>59</sup> software. The chemical phase diagrams for PipZnBr<sub>4</sub> and PipZnCl<sub>4</sub> were drawn by the Chesta<sup>60</sup> code.

### Defect calculations

For modeling the intrinsic defects in PipZnBr<sub>4</sub> and PipZnCl<sub>4</sub>, a  $2 \times 2 \times 2$  supercell containing 736 atoms and  $\Gamma$ -only  $k$ -mesh was used. The perfect and defect structures were fully relaxed by the GGA-PBE method until the total force on each atom was  $<0.03 \text{ eV \AA}^{-1}$ . The formation enthalpy ( $\Delta H_{D,q}$ ) for a defect (D) in a charge state  $q$  was calculated by refs. 61,62

$$\Delta H_{D,q} = E_{D,q} - E_h + q(E_v + E_f) + \sum n_i \mu_i + E_{\text{corr}} \quad (1)$$

where  $E_{D,q}$  is the total energy of the supercell containing the defect (D) in the charge  $q$ .  $E_h$  is the total energy of the perfect host supercell.  $E_v$  is the VBM level, while  $E_f$  is the Fermi level referred to  $E_v$ . The parameter  $n_i$  indicates the number of  $i$  atoms added ( $n_i < 0$ ) or removed ( $n_i > 0$ ) to form a defect (D).  $\mu_i$  is the chemical potential of the atom  $i$ .  $E_{\text{corr}}$  represents the total correction for  $\Delta H_{D,q}$ , including the band-filling correction, the potential alignment correction, and the image charge correction<sup>63,64</sup>. To address the band edge problem using the GGA-PBE method<sup>61,65</sup>, corrections were applied for both the valence band maximum (VBM) overestimation and the CBM underestimation. For PipZnBr<sub>4</sub>, the corrections are  $\Delta \text{VBM} = 0.89 \text{ eV}$  and  $\Delta \text{CBM} = 0.41 \text{ eV}$ , while for PipZnCl<sub>4</sub>, they are  $\Delta \text{VBM} = 1.02 \text{ eV}$  and  $\Delta \text{CBM} = 0.44 \text{ eV}$ . These corrections are incorporated by adding  $\Delta \text{VBM}$  (or  $\Delta \text{CBM}$ ) to the formation energy of deep acceptor (or donor) defects calculated using the HSE hybrid functional method. For shallow defects, the formation energy is adjusted to maintain its relative position to the edge. The charge transition level and the equilibrium Fermi level ( $E_{F,e}$ ) were

determined using methods identical to those employed in our previous research<sup>66</sup>.

### Zn-ion migration energy barrier calculations

The initial sites of the Zn-ion migration calculations were determined through numerous DFT energy calculations. Subsequently, the final position was identified as the symmetrical position in the corresponding direction of the supercell. For the migration energy barrier calculations along the  $a$ ,  $b$ , and  $c$  directions, supercells of dimensions  $2 \times 1 \times 1$ ,  $1 \times 2 \times 1$ , and  $1 \times 1 \times 2$  were employed, respectively. The diffusion pathways and barrier energies of Zn-ion diffusion throughout the PipZnBr<sub>4</sub> and PipZnCl<sub>4</sub> were calculated by using the CI-NEB<sup>30</sup> method implemented in VASP. The CI-NEB calculations, with a  $k$ -spacing of  $0.2 \text{ \AA}^{-1}$ , were determined to converge when the maximum force of each image was  $<0.03 \text{ eV \AA}^{-1}$ .

### Preparation of PipZnBr<sub>4</sub> solid electrolyte and electrode

**Preparation of PipZnBr<sub>4</sub>-based solid electrolyte.** The solid electrolyte was synthesized by hydrothermal method. Stoichiometric amounts of ZnBr<sub>2</sub> (over 98% purity, Shanghai Adamasi Reagents Co., Ltd.) and piperazine (over 99% purity, Shanghai Adamasi Reagents Co., Ltd.) were dissolved in hydrobromic acid (HBr, 48 wt %, Shanghai Aladdin Biochemical Technology Co., Ltd.). The mixture solution was added into the Teflon autoclave and was heated to  $90 \text{ }^\circ\text{C}$  within 120 min, and kept for 2440 min. Next, the reactor was cooled to  $25 \pm 0.5 \text{ }^\circ\text{C}$  within 1200 min. Finally, the solution was filtered and collected to yield the soft co-crystalline halides. Specifically, to synthesize PipZnBr<sub>4</sub> (1:1) and PipZnBr<sub>4</sub> electrolyte, including ZnBr<sub>2</sub> (0.6 mmol) and piperazine (0.6 mmol) or ZnBr<sub>2</sub> (3.0 mmol) and piperazine (0.6 mmol) were added in HBr (3 ml), respectively. Then the solution was transferred to a 20 ml Teflon autoclave. The as-synthesized PipZnBr<sub>4</sub> (1:1) and PipZnBr<sub>4</sub> powders were collected and stored in a 2 ml centrifuge tube for further characterization and electrochemical testing. To assemble the cell, the PipZnBr<sub>4</sub> powders were pressed at around 20 MPa for 2 min in a stainless steel mold ( $\phi = 16 \text{ mm}$ ) by Infrared Pellet Press (PC-30, Tianjin Jingtuo Instrument Technology Co., Ltd) under an air-conditioned room at  $25 \pm 0.5 \text{ }^\circ\text{C}$ . To evaluate the performance of the PipZnBr<sub>4</sub>-based solid electrolyte, the thickness of the electrolyte was controlled to approximately  $430 \text{ }\mu\text{m}$ . The reference  $1.2 \text{ M Zn(OTf)}_2$  electrolyte was prepared by dissolving Zn(OTf)<sub>2</sub> (98%, Shanghai Aladdin Biochemical Technology Co., Ltd.) in deionized water<sup>33</sup>. The hydrogel electrolyte was prepared according to reference<sup>34</sup>. First, gelatin (2 × g, 98%, Shanghai Aladdin Biochemical Technology Co., Ltd.) was dissolved in 40 ml deionized water under stirring at  $60 \text{ }^\circ\text{C}$  for 30 min. Subsequently, a specified quantity of oxidized dextran (OD) solution was introduced into the gelatin solution. The reaction system was then cooled below  $25 \pm 0.5 \text{ }^\circ\text{C}$  and held for 4 h to promote the coordination-driven modification of gelatin chain by OD. Following this, phosphate-buffered saline (20×, Shanghai Aladdin Biochemical Technology Co., Ltd.) was incorporated, and the mixture was stirred at  $60 \text{ }^\circ\text{C}$  for 1.5 h. Methacrylic anhydride (15%, w/v, Shanghai Aladdin Biochemical Technology Co., Ltd.) and the photo-initiator lithium phenyl-2, 4, 6-trimethylbenzoylphosphinate (LAP, 0.05% (w/v), 98%, Macklin, Shanghai Biochemical Technology Company) were added dropwise in sequence. The resulting prepolymer solution was dialyzed in water at  $40 \text{ }^\circ\text{C}$ , transferred into a polytetrafluoroethylene (PTFE) mold, and frozen at  $4 \text{ }^\circ\text{C}$ . Finally, the ODGelMA hydrogel film was obtained after drying and photocrosslinking under  $365 \text{ nm}$  UV light.

### Positive electrode preparation

The positive electrode was fabricated according to the method we reported earlier<sup>29,34</sup>. Carbon black (YP-50, Kuraray Co., Ltd), acetylene (Suzhou Siner Technology Co., Ltd), and PTFE powder (Guangdong Canrd New Energy Technology Co., Ltd.) with a mass ratio of 8:1:1 were mixed and hot-pressed onto a thin sheet (denoted as C). The as-

synthesized C and Ti mesh (100 mesh, Hebei Mengshang Metal Mesh Industry Co., Ltd) were pressed to build a positive electrode matrix (Ti@C). A mixed solution with iodine ( $I_2$ ) as active material was prepared by dissolving 1 M potassium iodide (KI, 99%, Shanghai Aladdin Biochemical Technology Co., Ltd.) and 0.5 M zinc sulfate ( $ZnSO_4$ , 99%, Shanghai Aladdin Biochemical Technology Co., Ltd.). Finally, the  $I_2$  electrode was obtained by depositing  $I_2$  onto the Ti@C at 5 mA for 6 min and dried at  $40 \pm 0.5$  °C for 24 h. The  $I_2$  loading mass is about  $3 \text{ mg cm}^{-2}$ .

### Characterizations

The structures of the PipZnBr<sub>4</sub> (1:1) and PipZnBr<sub>4</sub> solid electrolyte, as well as the electrode after cycling Zn plating/stripping, were characterized by FTIR spectra (AVATAR 370 mode) and Raman spectroscopy (523 nm, Horiba LabRAM HR800). The XRD (Rigaku, D/Max-2500) pattern was scanned from 5 to 80° with a Cu K $\alpha$  X-rays ( $\lambda = 1.5406$  Å) radiation at a scan rate of 10°/min and a step of 0.02°. The PipZnBr<sub>4</sub> solid-state electrolyte and the surface morphology of the Zn electrode were observed by SEM (Hitachi SU-4800 FE-SEM) with an EDS detector (Ultim Max 20) and EBSD (Nordlys Max 3 detection system) under the electron current of 13 pA and accelerating voltage of 2 kV. The surface feature of the cycled Zn electrode was observed by CLSM (Olympus LEXT OLS5000-SAF) and AFM (Bruker, Dimension icon). Chemical bonding information was obtained via XPS measurements performed on a PHI 5000 Versa Probe II spectrometer, utilizing monochromatized Al K $\alpha$  radiation for excitation. An integrated argon ion gun was utilized for sample sputtering, with a sputter rate calibrated against SiO<sub>2</sub> ( $25 \text{ nm min}^{-1}$ ) over a  $1 \times 1$  mm region. The C–C peak at 284.8 eV was used as a reference to calibrate the binding energies presented in this work. Non-destructive visualization of the solid-state battery's interior and the Zn electrode's deposition morphology was characterized using CT (Phoenix V MDTC-EQ-M60-01). The system operated at 140 kV and 180  $\mu$ A, capturing data at a 3  $\mu$ m spatial resolution with 334 ms exposures. A 3D reconstruction model and corresponding cross-sectional views were obtained by integrating the multi-angle scan datasets. The Zn element content in PipZnBr<sub>4</sub> (1:1) and PipZnBr<sub>4</sub> solid electrolyte was assessed in parallel three times by ICP (ThermoFisher iCAP Q). ATHENA software was used to process and normalize the XAFS spectra<sup>67</sup>. Wavelet transform analysis was then carried out on the EXAFS data employing the HAMA program.

### Electrochemical measurements

Zn foil (100  $\mu$ m, 99%, Wuhan Luojia Yanxin Technology Co., Ltd.) was polished with abrasive paper (20000 mesh) and cleaned with ethanol (AR, Shanghai Lingfeng Chemical Reagent Co., Ltd.) to remove the inactive layer. Zn foil was cut into a disc ( $\phi = 12$  mm) as an electrode. Ti foil (10  $\mu$ m, 99.99%, Wuhan Luojia Yanxin Technology Co., Ltd.) was cut into a disc ( $\phi = 16$  mm) to be applied as a positive electrode for Zn||Ti cells. All the testing CR2032 coin cells (stainless steel, Guangdong Canrd New Energy Technology Co., Ltd.) consisted of a stainless steel gasket (0.05 mm) and a shrapnel (0.1 mm), and they were assembled under a pressure of  $50 \pm 1 \text{ kgf cm}^{-2}$  in an open-air environment by using PipZnBr<sub>4</sub> solid electrolyte and tested on a battery test system (Neware) at  $40 \pm 1$  °C. All the batteries were subjected to electrochemical characterization without any additional pressure being applied. The GCD cycles of Zn|| $I_2$  using PipZnBr<sub>4</sub> solid electrolyte were conducted in a voltage range of 0.3–1.3 V ( $Zn^{2+}/Zn$ ). EIS tests were performed on a VSP-3e Potentiostat electrochemical workstation (BioLogic) operating in a potentiostatic mode. A frequency range of 100 kHz–50 MHz was explored, collecting 10 points per decade. To measure the EIS of the solid-state electrolyte at different temperatures, the electrolyte was measured in parallel three times. CV measurements were performed on Zn||Ti coin cells, employing 12 mm Zn foil and 16 mm Ti foil. The tests covered a potential range of –0.2 to 1.0 V at different scan rates

(0.1, 0.2, 0.5, and 1.0  $\text{mV s}^{-1}$ ) on an electrochemical workstation. The nucleation overpotential of the Zn electrode was studied on the electrochemical workstation based on the Zn|PipZnBr<sub>4</sub>|Zn cell. LSV test of Zn|PipZnBr<sub>4</sub>|Ti cell was conducted on workstations at  $1 \text{ mV s}^{-1}$  at –1.8–2.8 V. The Zn transference number is calculated by a current-time curve under constant polarization at –50 mV for 700 s. The Tafel profiles were operated on Zn|PipZnBr<sub>4</sub>|Ti cell. The ionic conductivity ( $\sigma$ ) of the as-synthesized PipZnBr<sub>4</sub> solid electrolyte was measured by EIS measurements. The  $\sigma$  was calculated based on the equation of  $\sigma = l/RS$ , where  $l$  represents the electrolyte thickness (430  $\mu$ m),  $R$  is the total impedance according to EIS measurement, and  $S$  is the area ( $2.0 \text{ cm}^2$ ). To gain the Arrhenius plots, carriage-temperature EIS was conducted from 0 to 60 °C. The activation energy ( $E_a$ ) was calculated on the Arrhenius equation. The cells were characterized in terms of their galvanostatic charge/discharge tests, CV curves, and rate performance using a 12-mm diameter Zn foil negative electrode and a  $1 \times 1$  cm  $I_2$  positive electrode with a controlled  $\sim 3 \text{ mg cm}^{-2}$ . The titanium mesh served as the substrate, with the  $I_2$  positive electrode material loaded on one side facing the solid-state electrolyte. Area current densities were calculated by the area of the negative electrode, while specific currents were determined based on the mass of iodine present in the positive electrode. All the assembled solid-state Zn cells with the sealing pressure of  $50 \pm 1 \text{ kgf cm}^{-2}$  were left for 6 h before the electrochemical test. Then, the cells underwent charging and discharging tests without any additional pressure being applied. At least ten cells were tested for a single electrochemical experiment to guarantee the reproducibility. The CE of a cell is the ratio of the discharge capacity to the charging capacity of the preceding charge cycle.

### Data availability

All data that support the findings of this study are available within the text, including the Methods, Supplementary Information, and Source data file. Raw datasets related to the current work are available from the corresponding author upon request. Source data are provided with this paper.

### References

1. Tian, Y. et al. Promises and challenges of next-generation “beyond Li-ion” batteries for electric vehicles and grid decarbonization. *Chem. Rev.* **121**, 1623–1669 (2020).
2. Yuan, Y. et al. Understanding intercalation chemistry for sustainable aqueous zinc–manganese dioxide batteries. *Nat. Sustain.* **5**, 890–898 (2022).
3. Wang, F. et al. Highly reversible zinc metal anode for aqueous batteries. *Nat. Mater.* **17**, 543–549 (2018).
4. Zampardi, G. & La Mantia, F. Open challenges and good experimental practices in the research field of aqueous Zn-ion batteries. *Nat. Commun.* **13**, 687 (2022).
5. Ma, L. et al. Realizing high zinc reversibility in rechargeable batteries. *Nat. Energy* **5**, 743–749 (2020).
6. Yu, X. et al. Ten concerns of Zn metal anode for rechargeable aqueous zinc batteries. *Joule* **7**, 1145–1175 (2023).
7. Zhong, W. et al. Mitigating cathodic dissolution through interfacial water masking to enhance the longevity of aqueous zinc-ion batteries. *Energy Environ. Sci.* **17**, 2059–2068 (2024).
8. Liang, Y., Qiu, M., Sun, P. & Mai, W. Comprehensive review of electrolyte modification strategies for stabilizing Zn metal anodes. *Adv. Funct. Mater.* **33**, 2304878 (2023).
9. Lv, Y., Xiao, Y., Ma, L., Zhi, C. & Chen, S. Recent advances in electrolytes for “beyond aqueous” zinc-ion batteries. *Adv. Mater.* **34**, 2106409 (2021).
10. Chen, Z. et al. Grafted MXene/polymer electrolyte for high performance solid zinc batteries with enhanced shelf life at low/high temperatures. *Energy Environ. Sci.* **14**, 3492–3501 (2021).

11. Su, Y. et al. Porous cyclodextrin polymer enables dendrite-free and ultra-long life solid-state Zn-I<sub>2</sub> batteries. *Angew. Chem. Int. Ed.* **62**, e202308182 (2023).
12. Zhi, J., Zhao, S., Zhou, M., Wang, R. & Huang, F. A zinc-conducting chalcogenide electrolyte. *Sci. Adv.* **9**, eade2217 (2023).
13. Lv, Z. et al. Stable solid-state zinc-iodine batteries enabled by an inorganic ZnPS<sub>3</sub> solid electrolyte with interconnected Zn<sup>2+</sup> migration channels. *Adv. Funct. Mater.* **34**, 2310476 (2023).
14. Luo, J. et al. Efficient and stable emission of warm-white light from lead-free halide double perovskites. *Nature* **563**, 541–545 (2018).
15. Feng, X. et al. Differential perovskite hemispherical photodetector for intelligent imaging and location tracking. *Nat. Commun.* **15**, 577 (2024).
16. He, B. et al. Halogen chemistry of solid electrolytes in all-solid-state batteries. *Nat. Rev. Chem.* **7**, 826–842 (2023).
17. Liang, Z. et al. Out-of-plane cations homogenise perovskite composition for solar cells. *Nature* **624**, 557–563 (2023).
18. Yin, Y.-C. et al. A LaCl<sub>3</sub>-based lithium superionic conductor compatible with lithium metal. *Nature* **616**, 77–83 (2023).
19. Asano, T. et al. Solid halide electrolytes with high lithium-ion conductivity for application in 4 V class bulk-type all-solid-state batteries. *Adv. Mater.* **30**, 1803075 (2018).
20. Slater, J. C. Atomic radii in Crystals. *J. Chem. Phys.* **41**, 3199–3204 (1964).
21. Müller, P. C., Ertural, C., Hempelmann, J. & Dronskowski, R. Crystal orbital bond index: covalent bond orders in solids. *J. Phys. Chem. C.* **125**, 7959–7970 (2021).
22. Schlem, R., Banik, A., Ohno, S., Suard, E. & Zeier, W. G. Insights into the lithium sub-structure of superionic conductors Li<sub>3</sub>YCl<sub>6</sub> and Li<sub>3</sub>YBr<sub>6</sub>. *Chem. Mater.* **33**, 327–337 (2021).
23. Bohnsack, A., Balzer, G., Güdel, H., Wickleder, M. S. & Meyer, G. Ternäre Halogenide vom Typ A<sub>3</sub>MX<sub>6</sub>. VII [1]. Die Bromide Li<sub>3</sub>MBr<sub>6</sub> (M=Sm–Lu, Y): Synthese, Kristallstruktur, Ionenbeweglichkeit. *Z. Anorg. Allg. Chem.* **623**, 1352–1356 (1997).
24. Li, X. et al. Water-mediated synthesis of a superionic halide solid electrolyte. *Angew. Chem. Int. Ed.* **58**, 16427–16432 (2019).
25. Bohnsack, A. et al. Ternäre Halogenide vom Typ A<sub>3</sub>MX<sub>6</sub>. VI [1]. Ternäre Chloride der selten-erd-elemente mit Lithium, Li<sub>3</sub>MCl<sub>6</sub> (M = Tb–Lu, Y, Sc): Synthese, Kristallstrukturen und Ionenbewegung. *Z. Anorg. Allg. Chem.* **623**, 1067–1073 (1997).
26. Wang, K. et al. A cost-effective and humidity-tolerant chloride solid electrolyte for lithium batteries. *Nat. Commun.* **12**, 1–11 (2021).
27. Chen, H., Wong, L. L. & Adams, S. SoftBV – a software tool for screening the materials genome of inorganic fast ion conductors. *Acta Crystallogr. Sect. B* **75**, 18–33 (2019).
28. Chen, H. & Adams, S. Bond softness sensitive bond-valence parameters for crystal structure plausibility tests. *Int. Union Crystallogr. J.* **4**, 614–625 (2017).
29. Lin, Y.-P. et al. Bright green emitter of Mn-doped C<sub>4</sub>H<sub>12</sub>N<sub>2</sub>ZnX<sub>4</sub> (X = Cl, Br) for X-ray radiography and WLEDs. *Chem. Eng. J.* **468**, 143818 (2023).
30. Henkelman, G., Uberuaga, B. P. & Jónsson, H. A climbing image nudged elastic band method for finding saddle points and minimum energy paths. *J. Chem. Phys.* **113**, 9901–9904 (2000).
31. Zanone, A., Tavares, D. T. & Paiva, J. L. D. An FTIR spectroscopic study and quantification of 2-amino-2-methyl-1-propanol, piperazine and absorbed carbon dioxide in concentrated aqueous solutions. *Vib. Spectrosc.* **99**, 156–161 (2018).
32. Hendra, P. J. & Powell, D. B. The infra-red and Raman spectra of piperazine. *Spectrochim. Acta* **18**, 299–306 (1962).
33. Chang, C. et al. A robust gradient solid electrolyte interphase enables fast Zn dissolution and deposition dynamics. *Energy Environ. Sci.* **17**, 680–694 (2024).
34. Kumankuma-Sarpong, J. et al. Entanglement added to cross-linked chains enables tough gelatin-based hydrogel for Zn metal batteries. *Adv. Mater.* **36**, 2403214 (2024).
35. Li, P. et al. MOF-derived defect-rich CeO<sub>2</sub> as ion-selective smart artificial SEI for dendrite-free Zn-ion battery. *Chem. Eng. J.* **451**, 138769 (2023).
36. Yan, J., Ye, M., Zhang, Y., Tang, Y. & Chao Li, C. Layered zirconium phosphate-based artificial solid electrolyte interface with zinc ion channels towards dendrite-free Zn metal anodes. *Chem. Eng. J.* **432**, 134227 (2022).
37. He, M. et al. Suppressing dendrite growth and side reactions on Zn metal anode via guiding interfacial anion/cation/H<sub>2</sub>O distribution by artificial multi-functional interface layer. *Energy Storage Mater.* **44**, 452–460 (2022).
38. Zhao, Y. et al. Tailoring grain boundary stability of zinc-titanium alloy for long-lasting aqueous zinc batteries. *Nat. Commun.* **14**, 7080 (2023).
39. Xie, C. et al. Discovering the intrinsic causes of dendrite formation in zinc metal anodes: lattice defects and residual. *Stress. Angew. Chem. Int. Ed.* **62**, e202218612 (2023).
40. Ma, G. et al. Zn metal anodes stabilized by an intrinsically safe, dilute, and hydrous organic electrolyte. *Energy Storage Mater.* **54**, 276–283 (2023).
41. Deng, D. et al. Ion tunnel matrix initiated oriented attachment for highly utilized Zn anodes. *Adv. Mater.* **35**, 230353 (2023).
42. Chi, S.-S., Qi, X.-G., Hu, Y.-S. & Fan, L.-Z. 3D flexible carbon felt host for highly stable sodium metal anodes. *Adv. Energy Mater.* **8**, 1702764 (2018).
43. Li, T. et al. Engineering fluorine-rich double protective layer on Zn anode for highly reversible aqueous zinc-ion batteries. *Angew. Chem. Int. Ed.* **62**, e202314883 (2023).
44. Fabini, D. H. et al. Dynamic stereochemical activity of the Sn<sup>2+</sup> lone pair in perovskite CsSnBr<sub>3</sub>. *J. Am. Chem. Soc.* **138**, 11820–11832 (2016).
45. Zhao, L. et al. Super chloride ionic conductivity in CsSnCl<sub>3</sub>-based perovskite compound and its application for solid-state chloride batteries. *adv. energy sustain. Res.* **5**, 2400198 (2024).
46. Frisch, M. et al. *Gaussian 16, Revision A.03* (Gaussian, Inc., Wallingford, CT, 2016).
47. Stephens, P. J., Devlin, F. J., Chabalowski, C. F. & Frisch, M. J. Ab initio calculation of vibrational absorption and circular dichroism spectra using density functional force fields. *J. Phys. Chem.* **98**, 11623–11627 (1994).
48. Weigend, F. & Ahlrichs, R. Balanced basis sets of split valence, triple zeta valence and quadruple zeta valence quality for H to Rn: design and assessment of accuracy. *Phys. Chem. Chem. Phys.* **7**, 3297–3305 (2005).
49. Grimme, S., Ehrlich, S. & Goerigk, L. Effect of the damping function in dispersion corrected density functional theory. *J. Comput. Chem.* **32**, 1456–1465 (2011).
50. Grimme, S., Antony, J., Ehrlich, S. & Krieg, H. A consistent and accurate ab initio parametrization of density functional dispersion correction (DFT-D) for the 94 elements H–Pu. *J. Chem. Phys.* **132**, 154104 (2010).
51. Lu, T. & Chen, F. Multiwfn: a multifunctional wavefunction analyzer. *J. Comput. Chem.* **33**, 580–592 (2011).
52. Humphrey, W., Dalke, A. & Schulten, K. VMD: visual molecular dynamics. *J. Mol. Graph.* **14**, 33–38 (1996).
53. Jain, A. et al. Commentary: the materials project: a materials genome approach to accelerating materials innovation. *APL Mater.* **1**, 011002 (2013).
54. Blöchl, P. E. Projector augmented-wave method. *Phys. Rev. B* **50**, 17953–17979 (1994).

55. Kresse, G. & Furthmüller, J. Efficient iterative schemes for ab initio total-energy calculations using a plane-wave basis set. *Phys. Rev. B* **54**, 11169–11186 (1996).
56. Perdew, J. P., Burke, K. & Ernzerhof, M. Generalized gradient approximation made simple. *Phys. Rev. Lett.* **77**, 3865–3868 (1996).
57. Nelson, R. et al. LOBSTER: local orbital projections, atomic charges, and chemical-bonding analysis from projector-augmented-wave-based density-functional theory. *J. Comput. Chem.* **41**, 1931–1940 (2020).
58. Krukau, A. V., Vydrov, O. A., Izmaylov, A. F. & Scuseria, G. E. Influence of the exchange screening parameter on the performance of screened hybrid functionals. *J. Chem. Phys.* **125**, 224106 (2006).
59. Momma, K. & Izumi, F. VESTA: a three-dimensional visualization system for electronic and structural analysis. *J. Appl. Cryst.* **41**, 653–658 (2008).
60. Chesta - Software for Creating Chemical Potential Diagrams. <https://n-hatada.github.io/chesta> (2024).
61. Lany, S. & Zunger, A. Assessment of correction methods for the band-gap problem and for finite-size effects in supercell defect calculations: case studies for ZnO and GaAs. *Phys. Rev. B* **78**, 235104 (2008).
62. Van de Walle, C. G. & Neugebauer, J. First-principles calculations for defects and impurities: applications to III-nitrides. *J. Appl. Phys.* **95**, 3851–3879 (2004).
63. Freysoldt, C., Neugebauer, J. & Van de Walle, C. G. Fully Ab initio finite-size corrections for charged-defect supercell calculations. *Phys. Rev. Lett.* **102**, 016402 (2009).
64. Kumagai, Y. & Oba, F. Electrostatics-based finite-size corrections for first-principles point defect calculations. *Phys. Rev. B* **89**, 195205 (2014).
65. Yuan, Z. et al. Engineering solar cell absorbers by exploring the band alignment and defect disparity: the case of Cu- and Ag-based kesterite compounds. *Adv. Funct. Mater.* **25**, 6733–6743 (2015).
66. Hu, S., Xia, B., Yan, Y. & Xiao, Z. Lead chloride perovskites for p-type transparent conductors: a critical theoretical reevaluation. *Phys. Rev. Mater.* **4**, 115201 (2020).
67. Ravel, B. & Newville, M. ATHENA, ARTEMIS, HEPHAESTUS: data analysis for X-ray absorption spectroscopy using IFEFFIT. *Synchrotron Radiat.* **12**, 537–541 (2005).

## Acknowledgements

The work was financially supported by the National Natural Science Foundation of China (52402325 awarded to S.H., 22402221 awarded to C.C.), Guangdong Basic and Applied Basic Research Foundation (2023A1515110588 awarded to S.H., 2024A1515010024 awarded to C.C.), the Shenzhen Science and Technology Program (RCYX20221008092934093 awarded to C.H., and JCYJ20230807140902005 awarded to S.H.), Guangdong Provincial Special Support Program (2023TQ07L367). The computing work associated with this paper was supported by the public computing service platform provided by SIAT.

## Author contributions

S.H. and C.C. conceived the ideas, designed and organized the research project under the supervision of K.Z., C.H., and H.C. S.H. did the theoretical calculations. Y.L. and X.L. synthesized the materials. C.C., Y.L., J.L., D.W., and X.L. did the materials characterizations. C.C., S.H., and Y.L. conducted the characterization analysis. S.H. and C.C. drafted and wrote the manuscript with data from all authors. H.C., C.H., K.D., S.H., C.C., and Y.L. revised the manuscript. All authors discussed the results and contributed to the manuscript.

## Competing interests

The authors declare no competing interests.

## Additional information

**Supplementary information** The online version contains supplementary material available at <https://doi.org/10.1038/s41467-026-68394-4>.

**Correspondence** and requests for materials should be addressed to Ke-Zhao Du, Hui-Ming Cheng or Cuiping Han.

**Peer review information** *Nature Communications* thanks the anonymous reviewer(s) for their contribution to the peer review of this work. [A peer review file is available].

**Reprints and permissions information** is available at <http://www.nature.com/reprints>

**Publisher's note** Springer Nature remains neutral with regard to jurisdictional claims in published maps and institutional affiliations.

**Open Access** This article is licensed under a Creative Commons Attribution-NonCommercial-NoDerivatives 4.0 International License, which permits any non-commercial use, sharing, distribution and reproduction in any medium or format, as long as you give appropriate credit to the original author(s) and the source, provide a link to the Creative Commons licence, and indicate if you modified the licensed material. You do not have permission under this licence to share adapted material derived from this article or parts of it. The images or other third party material in this article are included in the article's Creative Commons licence, unless indicated otherwise in a credit line to the material. If material is not included in the article's Creative Commons licence and your intended use is not permitted by statutory regulation or exceeds the permitted use, you will need to obtain permission directly from the copyright holder. To view a copy of this licence, visit <http://creativecommons.org/licenses/by-nc-nd/4.0/>.

© The Author(s) 2026